# *Fractional crystallization of high-K arc magmas: biotite- versus amphibole-dominated fractionation series in the Dariv Igneous Complex, Western Mongolia*

# Fractional Crystallization of High-K Arc Magmas: Biotite- vs. Amphibole-dominated Fractionation Series in the Dariv Igneous Complex, Western Mongolia

**Claire E. Bucholz[1*], Oliver Jagoutz[2], Max W. Schmidt[3], and Oyungerel Sambuu[4]**

[1]*Massachusetts Institute of Technology/Woods Hole Oceanographic Institution Joint Program in Oceanography, Cambridge, MA 02139, USA*

[2]*Department of Earth, Atmospheric, and Planetary Sciences Massachusetts Institute of Technology, Cambridge, MA 02139, USA*

[3]*Department of Earth Sciences, ETH, Zürich, Switzerland*

[4] *Mongolian University of Science and Technology, School of Geology and Petroleum Engineering, Ulaanbaatar, Mongolia*

*Corresponding Author:
Dept. of Earth, Atmospheric and Planetary Sciences, 54-1020
Massachusetts Institute of Technology
77 Massachusetts Avenue
Cambridge, MA 02139-4307
Tel.: +1 (617) 452-2784,
E-mail Address: cbucholz@mit.edu

**Abstract**

Many studies have documented hydrous fractionation of calc-alkaline basalts producing tonalitic, granodioritic, and granitic melts, but the origin of more alkaline arc-sequences dominated by high-K monzonitic suites has not been thoroughly investigated. This study presents results from a combined field, petrologic, and whole rock geochemical study of a paleo-arc alkaline fractionation sequence from the Dariv Range of the Mongolian Altaids. The Dariv Igneous Complex of Western Mongolia is composed of a complete, moderately hydrous, alkaline fractionation sequence ranging from phlogopite-bearing ultramafic and mafic cumulates to quartz-monzonites to late-stage felsic (63-75 wt.% $SiO_2$) dikes. A volumetrically subordinate more hydrous, amphibole-dominated fractionation sequence is also present and comprises amphibole(±phlogopite) clinopyroxenites, gabbros, and diorites. We present 167 whole rock analyses for the biotite- and amphibole-dominated series. First, we constrain the liquid line of descent (LLD) of a primitive, alkaline arc melt characterized by biotite as the dominant hydrous phase through a fractionation model that incorporates the stepwise subtraction of cumulates of a fixed composition. The modeled LLD reproduces the geochemical trends observed in the 'liquid'-like intrusives of the biotite series (quartz monzonites and felsic dikes) and follows the water-undersaturated albite-orthoclase cotectic (at 0.2-0.5 GPa). Second, as distinct biotite- and amphibole-dominated fractionation series are observed, we investigate the controls on high temperature biotite versus amphibole crystallization from hydrous arc melts. Analysis of a compilation of hydrous experimental starting materials and high-Mg basalts saturated in biotite and/or amphibole suggests that the degree of K-enrichment controls whether biotite will crystallize as an early high-T phase, whereas the degree of water

saturation is the dominant control of amphibole crystallization. Therefore, if a melt has the appropriate major element composition for early biotite and amphibole crystallization, as is true of the high-Mg basalts from the Dariv Igneous Complex, the relative proximity of these two phases to the liquidus depends on the $H_2O$-concentration in the melt. Third, we compare the modeled LLD and whole rock geochemistry of the Dariv Igneous Complex to the more common calc-alkaline trend. Biotite and K-feldspar fractionation in the alkaline arc series results in the moderation of $K_2O/Na_2O$ values and LILE concentrations with increasing $SiO_2$ as compared to the more common calc-alkaline series characterized by amphibole and plagioclase crystallization and strong increases in $K_2O/Na_2O$ values. Lastly, we suggest that common calc-alkaline parental melts involve addition of a moderate pressure, sodic, fluid-dominated slab component while more alkaline primitive melts characterized by early biotite saturation involve the addition of a high pressure potassic sediment melt.

*Key Words*: alkaline, biotite, cumulate, subduction zone, Mongolia

**Introduction**

Based on trace element similarities, it is well established that subduction-related magmatism is essential for the production of continental crust (CC). Understanding how primitive arc basalts evolve and form continental crust of an andesitic bulk composition, with granitic rocks dominating the upper CC, has been the focus of much research (Jagoutz and Schmidt 2012; 2013; Jagoutz 2010; Lee et al. 2007; Müntener and Ulmer 2006; Sisson et al. 2005). In general, two end member models have been proposed to produce silica-rich derivative liquids: (1) partial melting in the lower continental crust and (2) hydrous fractionation of Si-poor cumulates. Differentiating between these two end-member processes by only studying granites (or the residual/derivative liquids) is difficult as large degrees of fractional crystallization or small amounts of partial melting of basalt produce liquids of similar compositions. Indeed, Tuttle and Bowen (1958) lamented, "Field studies of granites deal with the end products of processes long since completed, and the most detailed mapping and study of these products may fail to give convincing evidence concerning the exact nature of the processes responsible for the relations." Since Tuttle and Bowen's early experimental work on granite genesis, however, several key field localities have been identified where relationships between cumulates/restites and derivative liquids have been observed. For primitive calc-alkaline magmas the importance of hydrous fractionation has been documented through careful study and analysis of preserved lower crustal paleo-arc sections of Kohistan (Pakistan) and Talkeetna (Alaska) (DeBari and Greene 2011; Greene et al. 2006; Jagoutz et al. 2011; Jagoutz 2010). In addition, experimental work on primitive basaltic melts have supported the evidence from the field (Grove et al. 2003; Müntener et al. 2001; Sisson and Grove 1993), indicating that in order to produce tonalites, granodiorites, and granites from primitive calc-alkaline basalts, cumulates dominated by $SiO_2$-poor minerals such as amphibole, garnet, oxides, or An-rich plagioclase must fractionate from the melt.

Although volumetrically less significant than calc-alkaline batholiths, the monzonitic series (monzodiorites, monzonites, and quartz monzonites) characterized by elevated total alkali contents at a given $SiO_2$ content, are widely present in arcs (e.g., Miller 1977; Miller 1978; Rapela and Pankhurst 1996; Sylvester et al. 1978). Due to their high $Na_2O+K_2O$ and LILE contents, they may constitute significant contributors to the incompatible element budget of the continental crust. Nevertheless, the origin of this monzonitic series has only been investigated in the field to a limited extent. Several field studies on high-K granitoids have suggested that biotite- and clinopyroxene-dominated fractionation from high-K primitive melts is capable of producing these derivative granitic liquids (Fowler and Henney 1996; Fowler et al. 2001; Lobach-Zhuchenko et al. 2008). However, these studies lack exposure of high-K ultramafic and mafic cumulates in significant enough quantities to substantiate the volumes required by their fractionation models. The only other field evidence for biotite+clinopyroxene fractionation from high-K primitive melts comes from the fragmentary evidence provided by phlogopite-bearing ultramafic cumulate xenoliths in high-K volcanics (Buhlmann et al. 2000; Downes et al. 2004; Giannetti and Luhr 1990).

Here, we present whole rock geochemical data for the recently discovered Dariv Igneous Complex (~50 $km^2$) in Western Mongolia, which is comprised of two distinct alkaline fractionation sequences. The first is a complete, moderately hydrous alkaline fractionation sequence ranging from phlogopite-rich ultramafic (wehrlites and clinopyroxenites) and biotite-rich mafic (monzogabbros and monzodiorites) cumulates through quartz-monzonites. The second, more incomplete sequence is comprised of isolated patches of amphibole(±phlogopite)-clinopyroxenites and stocks to km-sized intrusions of amphibole-bearing monzogabbros and (quartz-)monzonites. Through LLD modeling we show that evolved quartz-monzonites and felsic dikes associated with the biotite-dominated sequence can be produced through fractionation of the observed biotite-dominated cumulates from a primitive alkali-rich basalt. In light of the two fractionation sequences observed in Dariv (i.e., with early biotite versus amphibole saturation, respectively), we discuss the potential controls on high temperature amphibole and biotite crystallization in alkaline magmas with a particular emphasis on bulk magma chemistry and water content and highlight the effects of amphibole versus biotite crystallization on the fractionated melt chemistry. We then discuss the different subduction components influencing the mantle wedge and contributing to arc-related calc-alkaline versus high-K parental melts. The whole rock geochemistry and the modeled LLD are discussed in terms of the phase relationships in the quartz-K-feldspar-albite ternary and geochemical trends are compared to the more commonly studied calc-alkaline series.

**Geological Setting**

The Dariv Range is located in the Gobi-Altai Aimag (Province) of southwestern Mongolia and is part of the Mongolian Altaids. The Mongolian Altaids are part of the Central Asian Orogenic Belt (CAOB), a vast subduction complex that occupies a significant part of Asia, from the Urals to the Pacific Ocean and from the Siberian and Baltica cratons to the North China and Tarim cratons (Sengör et al.

1993). The Central Asian Orogenic Belt is comprised of amalgamated island arcs, ophiolites, accretionary wedges, and continental fragments that were accreted to the margin of Siberia beginning at *c.* 1.0 Ga and continuing until *c.* 250 Ma, when the Paleo-Asian ocean closed with the collision of the N. China craton along the southern Siberian margin (Buslov et al. 2001; Khain et al. 2003; Sengör et al. 1993; Sengör et al. 1994). The Dariv Range is located at the boundary between what we call here the Altai Allochthon, mostly composed of amphibolite- to granulite-facies Proterozoic metaigneous and metasedimentary lithologies, and the Lake Terrane, an Ediacaran-Early Paleozoic island arc system (Fig. 1a) (Badarch et al. 2002). The Lake Terrane is composed of ophiolites and arc-related plutonic and volcanic rocks, representing fragments of the Paleo-Asian ocean floor and an associated island arc systems (Khain et al. 2003). In the northern Dariv Range, six primary units are attributed to the Lake Terrane: (1) A mantle section (serpentinized harzburgite and dunite), which is intruded and overlain to the northwest by (2) an ophiolite sequence composed of gabbros, a dike complex, and lavas. The southern section of the ophiolite is intruded by an alkaline series ranging from (3) phlogopite-rich ultramafic and biotite-rich mafic cumulates to alkaline granitoids to (4) an amphibole-rich series of amphibole(±phlogopite) clinopyroxenites, hornblendites, amphibole-monzogabbros, –monzodiorites, and -monzonites that together are the primary focus of this study (Fig. 1b). The northern and western parts of the range are comprised of (5) Lake Zone volcanics/volcaniclastics and poorly-studied weakly metamorphosed igneous and sedimentary rocks, such as agglomerates and conglomerates. Lastly, a series of (6) large alkali-feldspar granites that intrude units 1-4 are also present (Fig. 1b). Rocks similar to units 1-4 and 6 are also found in the southern part of the Dariv Range, but the intrusive relationships have not been investigated as thoroughly (see Fig. 1c in Bucholz et al. (2014)). The few previous studies of the area have not recognized the hydrous magmatic sequences (3 and 4), but assigned them to the larger Dariv Ophiolite (also referred to as 'Bayannur' or 'Bayannor') ophiolite (Dijkstra et al. 2006; Khain et al. 2003; Kozakov et al. 2002; Kovalenko et al., 2014). Based on geochemical characteristics of the dike complex and gabbros, such as Nb-Ta depletions and enrichment in LILEs, the Dariv Ophiolite has been interpreted to have formed in a supra-subduction zone environment (Dijkstra et al. 2006).

**Field Relationships and Petrography**

Field relationships observed over four summers of fieldwork are described in detail in Bucholz et al. (2014), to which the reader is referred to for the field geology, including field photographs. We briefly present the salient features of the alkaline igneous complex of the northwestern part of the Dariv Range (Fig. 1b, Electronic Supplement Fig. 1-3).

A ~3.5 km wide ultramafic cumulate sequence is located within the central southern part of a 15 x 10 km serpentinized harzburgite/dunite body. The ultramafic cumulates are dominated by biotite-bearing lithologies, however there are minor volumes of amphibole(±biotite)-bearing ultramafic cumulates, which are described in more detail below. The contact between the serpentinite and the cumulate sequence is

marked by numerous small intrusions that cut into the serpentinite and are composed of cumulate minerals. A broadly systematic lithological variation is observed from northwest to southeast (Fig. 1c). Primitive wehrlites characterized by bright green Cr-diopside with minor phlogopite grade into biotite-dominated wehrlites and phlogopite-rich clinopyroxenites and biotite monzogabbros. Monzodiorite to quartz monzonite bodies are also present, sometime occurring as individual stocks cross-cutting other cumulate lithologies and other times gradually transitioning into the monzogabbros. Late stage 10-100 cm wide K-feldspar-rich felsic dikes and biotite-bearing basaltic dikes cross cut the cumulate sequence. Diffuse margins between the felsic dikes and monzonites indicate a comagmatic origin, whereas the margins of mafic dikes are sharply defined. Xenoliths of biotite cumulates and basaltic dikes are common in the monzonites. The serpentinite and both alkaline sequences are intruded by small (10-100 m in diameter) vertically oriented stocks and several large (up to 8 x 5 km wide) intrusions of alkali-feldspar-porphyric granite (Fig. 1b,c). Unpublished U-Pb zircon ages indicate that these (alkali-)granites are significantly younger than the alkaline complex and are neither cogenetic nor contemporaneous with the biotite-dominated lithologies. For this reason, we do not discuss them further.

The plutonic rocks with biotite as the dominant mafic, hydrous mineral comprise a common cumulate sequence resulting from a single LLD (Bucholz et al. 2014) and can be ascribed to a fractionation sequence defined by olivine + clinopyroxene ± Fe-Ti oxides → biotite + apatite → K-feldspar + plagioclase → amphibole + quartz. These rocks are generally very fresh and only clinopyroxene exhibits occasional alteration to actinolitic amphibole, particularly in the evolved rocks. None of the samples exhibit field or microstructural evidence of deformation.

The second sequence of alkaline cumulates, with amphibole as the primary hydrous mineral, is comprised of amphibole±biotite clinopyroxenites, hornblendites, amphibole-monzogabbros, -monzodiorites, and -monzonites which intrude both the biotite-dominated sequence and the serpentinite. The ultramafic cumulates occur as isolated outcrops or as centimeter- to meter-scale intrusions in the serpentinite each with variable modal abundances of constituent minerals. The feldspar-bearing lithologies are generally found as isolated stocks to km-scale intrusions intruding both the serpentinite and the biotite-dominated cumulate sequence (Fig. 1b,c). A detailed map showing the intrusive relationships of the evolved amphibole-bearing lithologies can be found in the Electronic Supplementary Material (Fig. 1-3). Monzodiorites and monzonites with amphiboles aligned due to magmatic flow are the predominant lithologies. These bodies are cross-cut by K-feldspar- and plagioclase-porphyric diorites to monzonites and numerous dikes, including felsic pegmatites, aplites, K-feldspar-plagioclase-quartz-porphyric felsic dikes, and basalts, which are mostly oriented E-W or NW-SE. Although cross-cutting relationships between the different dikes are complex in the field, it seems that the felsic and pegmatitic dikes are the oldest dikes as they are cross cut by the basaltic and K-feldspar porphyric dikes. Although the amphibole-dominated sequence is not continuous in the field, a general mineralogical progression can be observed from the ultramafic lithologies to the more-evolved, feldspar-dominated ones. For this

sequence, we infer a mineral crystallization order of clinopyroxene + apatite → amphibole + biotite → plagioclase + K-feldspar → quartz.

***Petrography of the Biotite-Dominated Fractionation Sequence***

*Wehrlites and Phlogopite Wehrlites*

The wehrlites are fine- to medium-grained (0.5-2 mm). The most primitive ($Mg\#^{bulk}$=85-91) phlogopite wehrlites consist of bright green clinopyroxene (~65%, all percentages in the text are modal) and olivine (25-30%) with intercumulus phlogopite[1] (2-10%) and occasional accessory titano-magnetite (Fig. 2a). Olivine occurs as subhedral to anhedral crystals that are commonly poikilitically enclosed within phlogopite. In some samples, olivine shows highly irregular margins surrounded by phlogopite. The modal percentage of phlogopite is variable in the wehrlites and gradually increases to a maximum of 45%, while that of olivine and pyroxene decrease (to <10% and to 45% respectively), resulting in a pronounced orthocumulate texture of olivine and clinopyroxene poikilitically enclosed within phlogopite (Fig. 2b).

*Phlogopite clinopyroxenites and phlogopitite*

The phlogopite clinopyroxenites are comprised of phlogopite, clinopyroxene, and apatite with accessory hemo-ilmenite, titanite, and zircon (Fig. 2c). In the clinopyroxenites, brown-reddish phlogopite grows interstitially between the clinopyroxene and occasionally encloses clinopyroxene. In one sample (MO-11-10), phlogopite is the dominant phase (~75%) and apatite becomes an important constituent (4-5%). Phlogopite occurs both as an intercumulus phase and as elongate light brown euhedral laths up to 1-2 mm in length with subhedral clinopyroxene and stout prismatic apatites. Apatites are poikilitically enclosed by both euhedral and intercumulus biotite.

*Biotite Monzogabbros*

Monzogabbros consist of alkali feldspar and plagioclase (together 28-50%), biotite (13-25%), and clinopyroxene (31-55%) with accessory subhedral sphene, apatite, zircon, and hemo-ilmenite (Fig. 2d). Biotite grows both interstitially and in large laths (1-2 cm in length), and may poikilitically enclose sphene and apatite. Oligoclase to andesine (An ~20-40) and K-feldspar occur together in subsolvus intergrowth. Apatite occurs as stubby, subhedral 1-2 mm long crystals.

*Clinopyroxene Monzodiorites to Quartz-Monzonites*

The monzodiorites, monzonites, and quartz-monzonites are composed of large K-feldspar megacrysts (1-2 cm in length) surrounded by smaller grains of K-feldspar and andesine (together 50-60%), quartz (10-20%), biotite (10-15%), amphibole (5-15%), and clinopyroxene (≤5%) with accessory apatite, sphene, zircon, and hemo-ilmenite. Biotite occurs as stubby laths, 1-4 mm in length. Clinopyroxene

[1] Throughout the text, we use 'phlogopite' when describing biotite in ultramafic lithologies and 'biotite' when describing biotite in feldspar-bearing lithologies.

contains both biotite and numerous apatite inclusions (5-100 μm diameter). Apatite is also enclosed in biotite.

***Amphibole-Dominated Fractionation Sequence Petrography***

*Amphibole Clinopyroxenites and Hornblendites*

Amphibole-bearing clinopyroxenites are comprised of subhedral, 1-2 mm interlocking pargasitic amphibole (~40-50%), 100-300 μm subhedral clinopyroxene (~40-50%), 20-100 μm elongated to stubby apatites (up to 5%), and minor magnetite (Fig. 2e-g). In some samples, minor andesine ($An_{45}$-$An_{35}$) and K-feldspar occur as interstitial anhedral grains. When present, phlogopite is a minor phase (<5 modal %), occurring as laths either enclosed in amphibole or interstitially. Apatite is generally poikilitically enclosed by amphibole. In some coarse-grained facies amphibole comprises up to 80% of modal mineralogy and reaches 3 cm in length, with more common dimensions of 1-2 cm.

*Amphibole Monzogabbros*

Monzogabbros generally display hypidomorphic equigranular textures with subhedral mm to cm-scale amphibole (~35-60%) surrounded by patchy intergrowths of K-feldspar and andesine (40-60%) and clinopyroxene (in part retrograded to actinolite) (<20%) (Fig. 2h). Biotite is often present, but limited to <10%. Accessory minerals include sphene, Fe-Ti oxides, and apatite. Apatite can be up to 1 mm in length and often occurs as inclusions within amphibole. Twinning within plagioclase is common.

*Amphibole-rich Granitoids*

Felsic intrusives of this series range from amphibole-bearing monzodiorites to quartz-monzonites. These intermediate to evolved lithologies are generally equigranular (though some more porphyric facies are present), and fine- to medium- grained. The rocks are generally undeformed, but locally display magmatic flow textures with distinct foliated appearance. Both plagioclase and K-feldspar occur as mm to cm scale phenocrysts and as smaller grains interlocking with quartz, amphibole, and biotite in the groundmass. Plagioclase often displays both Carlsbad and polysynthetic twinning. Accessory minerals include zircon, apatite, Fe-Ti oxides, and sphene.

***Late-Stage Amphibole and Biotite-Bearing Basaltic to Andesitic Dike Petrography***

Late stage basaltic to andesitic dikes that cross-cut the plutonic rocks of the alkaline fractionation series can be broadly grouped into three categories: 1) biotite-bearing, 2) amphibole-bearing, and 3) biotite- and amphibole-bearing. Group 1 dikes are comprised of phlogopite, plagioclase, and clinopyroxene with accessory apatite, zircon, and hematite. Phlogopite (50%) occurs in 100-200 μm long blocky laths often enclosing zircon and hematite. Subhedral, rounded 20-100 μm clinopyroxene crystals (5%) are surrounded by oligoclase-andesine ($An_{28}$-$An_{44}$) (45%). Plagioclase crystals display irregular margins and appear to have crystallized in between phlogopite. Zircon is an abundant accessory phase

occurring as 20-150 μm long prismatic crystals within both plagioclase and phlogopite. Group 2 amphibole-bearing dikes contain primarily amphibole (50-60%) and plagioclase (40-50%) in the groundmass with accessory Fe-Ti oxides and apatite. Groundmass amphibole is pale green, subhedral, and up to 300 μm in its longest dimension. Groundmass plagioclase has irregular margins, generally growing around amphibole. Up to 20 μm long euhedral, elongate apatite is poikilitically enclosed in plagioclase. In some dikes, amphibole and plagioclase occur as ~0.5-1 cm phenocrysts. Group 3 dikes are similar to Group 2 dikes in mineralogy and texture, however, biotite also occurs as a groundmass phase (10-15%) generally along the rims of amphibole.

**Analytical Methods**

168 whole rock major and trace element compositions are included in the presented data set. Most samples are from the northwestern part of the Dariv Range, though 14 are from the southeastern part of the range where a few similar alkali-rich lithologies are observed. Fresh pieces with no optical indication of weathering or veining were cut from samples to ensure uncontaminated and representative chemical analyses. Samples were powdered in an agate mill, which was cleaned with silica sand in between samples. The powders were then dried overnight at 105ºC. Loss on ignition was determined from mass loss after heating to 1050ºC for most samples and to 950ºC for samples with high silica contents. Glass discs were prepared using a lithium tetraborate flux. Major elements were measured using a wave-length dispersive X-ray fluorescence (XRF) spectrometer at ETH in Zürich. Trace elements of the fusion discs were determined by laser ablation inductively coupled plasma mass spectrometer (LA-ICPMS) at ETH. The XRF glass discs were broken and analyses were performed on freshly broken surfaces. Samples were loaded along with the NIST610 glass standard and a lithium tetraborate blank in an ablation cell and the ablated material was transported to the ICP-MS by a He carrier gas. The ablation system consists of a 193 nm ArF Excimer laser (Lambda Physik) with a homogenized beam profile connected to an Elan6100 DRC quadrupole ICP-MS. The background was measured for ~40 s prior to each analysis and the laser signal was integrated over 40-50 s. Using a 90 μm laser spot size, a minimum of 3 shots per disc were done to ensure homogeneity of the analyzed pellet. The analytical set-up was tuned for optimum performance across the entire mass range and daily optimization of the analytical conditions were performed to ensure a ThO production rate of below 0.2% (i.e. Th/ThO intensity ration <0.002). and a Th/U sensitivity ratio of 1 measured on the NIST610 glass standard. Two analyses on the NIST610 standard at the beginning and end of each set bracketed up to 20 analyses of unknowns. The blank was measured at the beginning of each session and its spectrum subtracted from the unknown spectra. The NIST610 standard was used as an external standard to calibrate analyte sensitivities and to correct for linear drift during analyses. Data reduction of LA-ICP-MS analyses followed the procedures described in Longerich et al. (1996). CaO was used as the internal standard element to correct for matrix effects and calculate trace element concentrations.

## Whole Rock Geochemistry

### *Major Element Chemistry*

GPS locations and whole rock major and trace element chemistry of the analyzed samples are provided as Electronic Supplementary Material. Based on total major element chemistry and modal mineralogy, both the biotite- and amphibole-dominated series follow a calc-alkaline trend. The feldspar-bearing rocks belong to the sub-alkalic trend of monzogabbros, monzodiorites, and (quartz-) monzonites (Fig. 3c) (Lameyre and Bowden 1982). Following the classification of Frost et al. (2001), the monzodiorites, monzonites, and quartz-monzonites are meta-aluminous, magnesian, and belong predominately to the alkali-calcic trend using the modified alkali-lime index (MALI: $Na_2O + K_2O - CaO$). The late-stage felsic dikes are metaluminous to slightly peraluminous ($0.95 < Al/(Ca-1.67P+Na+K) <1.1$) and predominantly magnesian.

#### *Biotite-Dominated Sequence*

With progressing fractionation, the Mg# (molar $Mg/(Mg+Fe^T)$ x 100) decreases from the most primitive ultramafic cumulates to the evolved (quartz-)monzonites (Fig. 3a). The major element chemistry of the ultramafic cumulates mainly depends on the mode of olivine, clinopyroxene and biotite. The phlogopite -free wehrlites contain 47-52 wt.% $SiO_2$, 1.0-1.5 wt.% $Al_2O_3$ and almost no $K_2O$, while the phlogopite clinopyroxenites have 43-52 wt.% $SiO_2$, 3.1-10.7 wt.% $Al_2O_3$ and up to 4.4 wt% $K_2O$ (Fig. 3b,d). $SiO_2$ increases with the increasing abundance of feldspar in the monzogabbros and more evolved rocks to ~63 wt.% in the monzonites and to 70-75 wt.% in the late-stage granitic dikes. CaO decreases constantly with decreasing Mg#, due to the decrease in modal abundance of clinopyroxene and the decrease in anorthite content in plagioclase with progressive fractionation. $Al_2O_3$ contents peak at ~19 wt.% in the monzodiorites and quartz-monzonites due to the abundance of feldspar (Fig. 3b). The felsic dikes are consistently lower in $Al_2O_3$ than the most evolved monzonites (14-16 wt.%). $Na_2O$ contents remain low in the ultramafic cumulates (<0.3 wt.%) and do not increase much until alkali-feldspar becomes a fractionating phase. Total alkalis reach 8 wt.% in the quartz monzonites (Fig. 3c). Due to its compatibility in biotite, $TiO_2$ is strongly controlled by biotite mode in the ultramafic cumulates, increasing from the phlogopite-poor to the phlogopite-rich cumulates and reaching 2.7 wt.% in the phlogopitite. $TiO_2$ then decreases with increasing $SiO_2$ in the monzogabbros and the monzonites (Fig. 3e). $P_2O_5$ contents in the ultramafic cumulates are controlled by apatite abundance with a maximum of 1.4 wt.% $P_2O_5$ in the apatite-rich phlogopitite sample, but decrease steadily with increasing degree of fractionation.

#### *Amphibole-Dominated Sequence*

The major element chemistry of the ultramafic amphibole cumulates mainly depends on the mode of clinopyroxene, amphibole, and, to a lesser extent, biotite. Only two primitive amphibole (+ minor

phlogopite) clinopyroxenites (MO-10-398 and MO-10-373) were identified with Mg#'s of 85-86, $SiO_2$ contents of 53.5 wt.%, and $Al_2O_3$ of 1.7-3.4 wt.%. The next most primitive amphibole clinopyroxenites have Mg#s of 67-73 and $SiO_2$ contents of 48.5-52.8 wt.%. As the mode of hornblende increases, the Mg# of the cumulates decreases to ~50 and $SiO_2$ contents decrease to 38.1 wt.% in the hornblendites. In the amphibole-rich clinopyroxenites, $Al_2O_3$ contents are 7.9-12.5 wt.% (Fig. 3b) and FeO concentrations are high (10.4-18.3 wt.%). $K_2O$ contents are lower in the amphibole-dominated clinopyroxenites than in the phlogopite-rich ultramafic lithologies, varying between 0.5 and 2.0 wt.% (Fig. 3d). Conversely, $Na_2O$ contents are higher in the amphibole clinopyroxenites (2.4-4.7 wt.%.) than in the phlogopite clinopyroxenites. With the onset of feldspar crystallization in the amphibole gabbros and diorites, $SiO_2$ increases to 53.9 and 59.8 wt.%. In the more evolved rocks, $Al_2O_3$ contents are primarily a function of feldspar mode and reach a maximum of 19.5 wt.% in an amphibole gabbro (Fig. 3b). CaO decreases constantly with decreasing Mg#, due to the decrease in modal abundance of clinopyroxene, with the amphibole clinopyroxenites and monzogabbros containing 11.9-16.0 wt.% and 5.1-9.6 wt.% CaO, respectively. $TiO_2$ concentrations are the highest in the amphibole clinopyroxenites (reaching 2.9 wt.% in sample MO-10-328) and generally decrease with increasing $SiO_2$ (Fig. 3e). $P_2O_5$ contents are generally high (up to 2.1 wt.%) in the amphibole clinopyroxenites due to high modal abundances of apatite, but then decrease with progressive fractionation.

***Trace Element Chemistry***

*Biotite-Dominated Sequence*

Ni and Cr are positively correlated with Mg# and strongly decrease with differentiation. This trend is concordant with early fractionation of olivine, clinopyroxene, and minor Cr-spinel. Ba enrichment in the ultramafic cumulates is controlled by phlogopite abundance, reaching 2290 ppm in the phlogopitite with 60 modal % phlogopite. In the evolved rocks, Ba concentrations remain uniformly high (750-1500 ppm) due to its compatibility with alkali feldspar. Rb follows trends similar to Ba. The ultramafic rocks mostly exhibit depleted Pb and Sr signatures and depletion in the HREE relative to LREE ($(La/Yb)_N$ = 2-12), (Fig. 4a-d). The more evolved feldspar-bearing rocks exhibit positive Pb anomalies and enrichment in LILEs, (Fig. 4e-h). No Eu enrichment is present in monzodiorites to quartz-monzonites, but there is strong Sr enrichment due to the presence of oligoclase to andesine ($An_{16-40}$) in these rocks (Fig. 4f,g). The evolved rocks are more enriched in LREE than the wehrlitic cumulates ($(La/Yb)_N$ = 8-25) (Fig. 4). Trace element patterns normalized to primitive mantle for the biotite-dominated sequence exhibit depletions in Nb, Ta, Zr, and Hf except for the quartz monzonites which have normalized Zr and Hf concentrations comparable to other incompatible elements (Fig. 4). Th and U are depleted in most, but not all, phlogopite-rich ultramafic cumulates and monzonites, while there is no distinct depletion in the felsic dikes.

*Amphibole-Dominated Sequence*

Ni and Cr contents are highest in the ultramafic cumulates (up to 208 and 1790 ppm, respectively) and are positively correlated with Mg#. Ba and Rb contents in the ultramafic lithologies of the amphibole-dominated sequence are controlled by the modal abundance of biotite and are therefore generally lower than that of the biotite-only fractionation sequence (Fig. 5a). The ultramafic amphibole-bearing cumulates are variably enriched or depleted in Pb with respect to other incompatible elements, have negative Sr signatures, and are depleted in HREE relative to LREE ($(La/Yb)_N$ = 7-22) (Fig. 5a). No Eu enrichment is present in the amphibole monzogabbros or diorites, but they generally exhibit a strong enrichment in Sr (Fig. 3f, 5b,c). The feldspar-bearing lithologies show a similar to slightly greater enrichment in LREE to HREE as the ultramafic cumulates ($(La/Yb)_N$ = 5-49) (Fig. 5). The feldspar-bearing amphibole monzogabbros and granitoids exhibit enrichments in Pb and LILE relative to other incompatible elements (Fig. 5b,c). Nb, Ta, Th, and U are all depleted relative to other incompatible elements, while Zr and |Hf are depleted in the ultramafic cumulates and monzogabbros but not in the more Si-rich intrusives

## Discussion

### *Liquid Line of Descent (LLD) Modeling – Biotite-Dominated Series*

Field relationships clearly indicate that quartz-monzonites that have biotite as the predominant hydrous mineral are intimately related to the biotite-dominated cumulate sequence (Bucholz et al. 2014). Therefore, in order to test whether these evolved quartz-monzonites and late stage felsic dikes could be produced by fractionation of the biotite-bearing ultramafic and mafic cumulates from a primitive melt, we model the LLD and compare the results to bulk rock analyses. We do not model the LLD of the amphibole-dominated sequence due to the lack of primitive amphibole cumulates (Fig. 3a) and the incomplete characterization of more primitive fractionating lithologies.

#### *Model Description*

The LLD of the magma parental to the biotite-series cumulates was modeled by stepwise subtraction of cumulates of fixed composition following the method described in Jagoutz (2010) (see his equation 1). Fractionation steps were 1%. This model was chosen over more traditional methods utilizing mineral-melt partition coefficients and corresponding equations for fractional or equilibrium crystallization because the fractionating lithologies and the parental melt composition could be constrained from field observations and chemical analyses. In addition, this method is also independent of the choice of partition coefficients and fractionation mechanism (i.e. fractional versus equilibrium crystallization). The parental melt composition was constrained by averaging the composition of three primitive (Mg# = 67-74, Ni = 144-171 ppm, and Cr = 520-643 ppm) late-stage basaltic dikes with biotite as phenocrysts or in the groundmass that cross-cut the cumulate sequence (samples MO-11-19, MO-9-228, MO-9-230). These synmagmatic dikes have phenocrysts and groundmass mineralogy similar to the

cumulate sequence (e.g., biotite and clinopyroxene) and trace element concentrations that are in equilibrium with clinopyroxenes from the most primitive phlogopite wehrlites (Bucholz et al., 2014). The range of compositions of these dikes corresponds to a K-rich basalt ($Na_2O$ = 1.84-2.66 wt.%, $K_2O$ = 1.63-2.76 wt.%, 48.7-52.9 wt.% $SiO_2$).

Fractionating compositions were constrained by averaging 1 to 7 samples of representative cumulative lithologies (Table 1). Unaltered dunite (±clinopyroxene ±phlogopite) with clear relationships to the biotite fractionation sequence was not observed in the field, but such dunites have been documented as xenoliths in alkali magmas and early olivine-only crystallization intervals are observed in crystallization experiments on high-K melts (e.g., Righter & Carmichael, 1996). As the most primitive wehrlite sampled is in equilibrium with a melt of Mg# ~66 (all Fe as ferric Fe), we included 5% fractionation of the average of phlogopite-bearing dunite cumulate xenoliths from the Bear Paw Mountains (Downes et al. 2004) to account for the gap between the primitive melt (Mg# 71.6) and a melt in equilibrium with the Dariv wehrlites. We chose these dunites as a range of phlogopite-bearing ultramafic cumulate xenoliths similar to the sequence in Dariv is observed in the Bear Paw Mountains (e.g., phlogopite wehrlites and clinopyroxenites) suggesting a similar crystallization sequence.

Evolved plutonic rocks may range from segregated cumulates to solidified bulk melts, which may be inferred from trace element systematics, such as positive or negative Eu anomalies. Although the evolved rocks do not display a positive Eu anomaly, this is not evidence against feldspar accumulation as all Eu was $Eu^{3+}$ at the moderately elevated oxygen fugacity of +2 to +3 ΔFMQ (log-units above the fayalite-quartz-magnetite buffer) in this fractionation sequence (Bucholz et al. 2014). Instead, elevated Al/Si (>0.17) and Sr/Nd (>27) ratios were taken to indicate accumulation of feldspar and were used to identify the monzogabbros, monzodiorites, and monzonites of cumulate character.

As the areal extent of the various cumulate lithologies in the field is not necessarily representative of total volumes, the mass of each cumulate type crystallized was estimated by utilizing cumulate olivine and clinopyroxene Mg# to calculate the equilibrium melt Mg# and comparing that to the modeled melt Mg# (e.g., Greene et al. 2006) (Fig. 6). With approximately 35% of the total melt Fe present as $Fe^{3+}$ (at the oxygen fugacity of the ultramafic cumulates of +2 to +3 Δ QFM (Bucholz et al., 2014)), the modeled melt Mg# is similar to slightly lower than the melt Mg# calculated to be in equilibrium with olivine- and clinopyroxene from the cumulates (using $K_D^{Fe\text{-}Mg}$(olivine-melt) = 0.3 (Roedder & Emslie, 1970) and $K_D^{Fe\text{-}Mg}$(clinopyroxene-melt) = 0.23) (following findings of Sisson & Grove, 1993). In general, calculated equilibrium melt Mg# (including the Fe oxidation state adjustment) for the ultramafic cumulates range from ~70 to 55. We therefore allow for an interval of ultramafic cumulate fractionation until the modeled LLD Mg# reaches ~60. The equilibrium melt Mg# calculated from clinopyroxenes in the more evolved cumulates (monzogabbros, monzodiorites, and monzonites) is lower than that of the modeled LLD. This could be due to uncertainties in the oxidation state of these lithologies or the limited number of samples with clinopyroxene analyses. Within the constraints of Fe-Mg partitioning between melt and crystallizing

phases, the amount of each cumulate type was varied iteratively until an optimal fit between the modeled LLD and more evolved lithologies was achieved. The final model fit yields the following cumulate mass percentages: 5% dunite, 3% wehrlite, 5% phlogopite-poor wehrlites (<0.3 wt.% $K_2O$ in the bulk cumulate), 10% phlogopite-rich wehrlites (>0.7 wt.% $K_2O$ in the bulk cumulate), 8% phlogopitite, 21% high Mg# monzogabbro (bulk Mg# > 65), 14% low Mg# monzogabbro (bulk Mg# < 59), 26% monzodiorite, 5% monzonite. Calculations were performed until 5% liquid mass remained. Furthermore, the composition of the average primitive melt from the three biotite-bearing primitive dikes was modified within error in order to optimally reproduce the geochemical trend defined by the bulk rocks. Oxides or trace elements were not modified more than ±25% of the average, with most to <10% and well within the $2\sigma_{SD}$ of the primitive dikes' average. Assimilation was not considered in the model, but we cannot exclude a minor contribution of this mechanism to the evolving plutonic series.

Uncertainties associated with this modeling approach are discussed in detail by Jagoutz (2010) and include variability in the composition of the primitive parental melt, estimates of the mass fraction of each cumulate type crystallized, and the degree to which the samples used in the average bulk cumulate compositions are representative of the actual fractionating compositions and chemical variability in a given lithology. Our methods of reducing the first two uncertainties are discussed above and we use the best estimates possible from the available constraints. The last source of uncertainty is inherent to a finite whole rock geochemical dataset, but is mitigated by our division of cumulate lithologies into nine coherent geochemical groups.

*Model Results*

The major and trace element compositions of the derivative melt at 10% fractionation intervals are given in Table 2 and the calculated LLD and fractionated cumulate compositions are shown in Figs. 3, 6, & 7. Beginning with a primitive alkali-rich basalt composition, the model successfully reproduces the major and minor trace element characteristics observed in the most evolved monzonites and late-stage felsic dikes.

*$SiO_2$ Enrichment*

A general difficulty in producing silica-rich granitoids by magmatic differentiation alone is that fractionation of gabbros, which have similar $SiO_2$ contents as basaltic to basaltic andesite melts (48-54 wt%), is inefficient for producing volumetrically significant silica-rich derivative liquids (Annen et al. 2006; Jagoutz 2010). Thus, early appearance of plagioclase and clinopyroxene as fractionating phases does not result in the silica-enrichment observed in upper crustal granitoids. Rather, silica-enrichment requires the fractionation of cumulates dominated by $SiO_2$-poor minerals. For calc-alkaline basalts, the importance of hydrous, high-P fractionation of silica-poor minerals such as amphibole, garnet, oxides, and An-rich plagioclase is well documented experimentally (Müntener et al. 2001; Grove et al. 2003; Sisson et al. 2005; Alonso-Perez et al. 2009) and from field studies (Greene et al. 2006; Jagoutz et al. 2010; Dessimoz et al. 2012). For the high-K parental basalt in Dariv, the primary fractionating low $SiO_2$

mineral is biotite, (with ~35 wt.% $SiO_2$). The phlogopite-rich wehrlites and phlogopitites have the required low $SiO_2$ contents and their fractionation produces sufficient silica enrichment such that subsequent fractionation of monzogabbros and monzodiorites results in further $SiO_2$ enrichment (Figs. 3 & 6). The model reproduces the silica-content of the least evolved monzonites (55-60 wt.% $SiO_2$) with 24-63% melt remaining. The most evolved quartz-monzonites and late stage felsic dikes (63-75 wt.% $SiO_2$) can be produced through fractionation of cumulates when ≤16% of the melt remains. This amount of melt is in reasonable agreement with the volumes of (quartz-)monzonites and felsic dikes observed in the field. Interestingly, whereas moderate to high pressure fractionation has been demonstrated as an effective mechanism to produce $SiO_2$ enrichment in calc-alkaline basalts (Alonso-Perez et al. 2009; Jagoutz et al. 2011; Müntener et al. 2001), the fractionation sequence observed in Dariv occurred at relatively low pressures (< 0.2-0.4 GPa, Bucholz et al. 2014[2]) and still resulted in significant $SiO_2$-enrichment. This is primarily due to the stability of biotite on the liquidus of these melts, but also to the protracted fractionation of olivine resulting from a stability field increasing with decreasing pressure (Esperança and Holloway 1987; Righter and Carmichael 1996).

*Other Major Elements*

It is illustrative to inspect the behavior of several key oxides to determine the proportion and composition of cumulate lithologies as well as the parental magma composition. $Al_2O_3$ enrichment of fractionating melts to levels not observed in arc granitoids is a common problem in models of primitive arc magma fractionation (Annen et al. 2006; Blatter et al. 2013). One way to limit $Al_2O_3$ enrichment is for fractional crystallization to occur at greater pressures. Higher $pH_2O$ stabilizes garnet (e.g., Alonso-Perez et al. 2009; Wolf and Wyllie 1994), aluminous amphibole (Grove et al. 2003) and anorthite-rich plagioclase (34-36 wt.% $Al_2O_3$) which all minimize $Al_2O_3$ enrichment in fractionating magmas (Annen et al. 2006; Jagoutz 2010). Nevertheless, it has been noted that deeper fractionation results in a larger interval of clinopyroxene crystallization and therefore an increases in the aluminum saturation index (ASI = Al/(2Ca+Na+K)) (Blatter et al., 2013). In Dariv, however, the observed alkaline sequence crystallized at relatively low pressures (0.2-0.4 GPa, Bucholz et al. 2014) and amphibole, garnet, and anorthitic plagioclase are not important fractionating phases in the biotite+clinopyroxene-dominated series. Due to its relatively high Al contents (13.5-16.8 wt.%), biotite crystallization limits Al-enrichment to some extent. The whole rock $Al_2O_3$ contents of the phlogopite ultramafic cumulates (1.0-10.8 wt.%, Fig. 3b), however, are still low compared to high pressure hornblendite and garnetite cumulates from other paleo-arc sequences (e.g., 15.0-22.5 wt.% $Al_2O_3$ (Jagoutz 2010)) and a further mechanism is required to limit Al-enrichment. An alternative would be a primitive melt that itself has relatively low $Al_2O_3$ (Annen et al. 2006). Primitive arc basalts have highly variable $Al_2O_3$ contents of 10-18 wt.% with most between 14-16 wt.%. Primitive high-K basalts from Dariv have $Al_2O_3$ contents between 12.3-15.3 wt.%. Using a slightly

[2] Note that the errors of the Al-in-hornblende pressures of Table 2 in Bucholz et al. (2014) were reproduced incorrectly, the correct values are 0.15±0.08, 0.21±0.05, 0.20±0.10, 0.24±0.05, 0.15±0.02, and 0.34±0.02 GPa.

lower $Al_2O_3$ content (12.9 wt.%) than the average primitive basalt composition, Al-enrichment is sufficiently limited and the observed geochemical trends are reproduced well (Fig. 3b).

A decrease in $TiO_2$ with $SiO_2$-enrichment is observed in Dariv and other arc suites (Dessimoz et al. 2012; Greene et al. 2006; Jagoutz 2010). Initially, however, $TiO_2$ is incompatible during the fractionation of olivine- and pyroxene-rich cumulates. The observed decrease in $TiO_2$ must therefore be explained by crystallization of a $TiO_2$-rich phase. In the Kohistan and Talkeetna paleo-arcs amphibole and Fe-Ti oxides had sufficiently high $TiO_2$-contents to produce a decrease in $TiO_2$ concentrations with increasing fractionation (Greene et al., 2006; Jagoutz, 2010). In Dariv, the early crystallizing phlogopite has 2.1-4.9 wt.% $TiO_2$ and phlogopite-rich wehrlites and phlogopitites have the required high $TiO_2$ contents (1.3 and 2.8 wt.% on average, respectively), to drive fractionating liquids to lower $TiO_2$ contents (Fig. 3e). In addition, accessory titanomagnetite (3.5-23.0 wt.% $TiO_2$, Bucholz et al. 2014) contributes to the high $TiO_2$ concentrations of the phlogopite-rich wehrlites and phlogopitites.

The high $K_2O$ contents of several of the fractionating lithologies (e.g., phlogopitite, monzonite) necessitate a primitive starting composition with high $K_2O$ in order to yield the elevated $K_2O$ contents of the quartz-monzonites and late-stage felsic dikes. As we only have one phlogopitite sample (MO-11-10), it is somewhat uncertain how representative its $K_2O$ content (4.5 wt.%) is of the actual fractionating composition. For example, 4.5 wt.% $K_2O$ is high compared to the average 3.4 wt.% $K_2O$ of phlogopite clinopyroxenite xenoliths from other localities. If the latter $K_2O$ value is used, a primitive melt with 2.96 wt.% $K_2O$ yields the $K_2O$ concentrations of the late stage felsic dikes (Fig. 3d). This value is similar to two of the K-rich primitive dikes (2.8 wt.% $K_2O$). Therefore, we treat 2.96 wt.% $K_2O$ in our primitive melt as the value necessary to reproduce the trends observed in the most silica-rich dikes.

*Trace Elements*

Fractionation of a few percent of dunite is required to reproduce the Ni contents of the most magnesian olivines (1135±82 ppm, Bucholz et al. 2014), which are lower than typical mantle olivine values (3500-4500 ppm) (Arai 1994; Sato 1977). Cr and Ni then decrease dramatically in the evolving melt with fractionation of olivine-rich wehrlites. LILE concentrations in the Dariv primitive melts are high (Ba: 561-1007 ppm; Rb: 30-79 ppm). Rb increases with progressive fractionation due to the high initial concentration of the primitive melt and comparatively low concentrations in the fractionating cumulates. Ba is 1.5-13 times more compatible than Rb in biotite crystallizing from alkali basalts, (Green et al. 2000; LaTourrette et al. 1995; Villemant et al. 1981) and therefore displays more gentle enrichment trends. All REE follow a similar trend. Initially they are incompatible in the olivine and biotite-dominated ultramafic cumulates and therefore increase in the fractionating melt. In the apatite-bearing cumulate assemblages, however, REE become compatible and their concentrations in the melt begin to decrease. REE concentrations of the "liquid-like" granitoids and felsic dikes are best reproduced between 20-40% and 10% melt remaining, respectively (Fig. 7). Sr displays a similar pattern, but decreases in evolved

liquids due to plagioclase fractionation in the monzogabbros and monzodiorites (Fig. 3f). Nb and Ta concentrations are high in the primitive melt (~9 ppm, 0.53 ppm) and increase moderately with continued fractionation. Although the wehrlites and dunites contain little Nb or Ta, they are compatible in biotite, which moderates Nb and Ta enrichment in the evolving melt. For example, the phlogopitite and other phlogopite-rich cumulate xenoliths contain 2-7 ppm Nb.

### *Biotite- and Amphibole-Series in Arcs*

*Controls on Biotite and Amphibole Crystallization in Hydrous Arc Melts*

In the Dariv Igneous Complex, two distinct alkaline fractionation sequences are observed: one with early saturation of biotite and much later crystallization of amphibole and the second with early saturation of amphibole accompanied by minor biotite. As such, an important question to address is which parameters control high temperature, early crystallization of biotite and/or amphibole in hydrous arc-related basalts. To investigate the influence of melt composition and $H_2O$-content we compiled major element data from experiments on hydrous basaltic to andesitic starting materials and from natural high Mg# (>60) alkali-basalts and lamprophyres from the Mexican Volcanic Belt saturated with (i.e., had phenocrysts of) amphibole and/or biotite (Figs. 8 & 9). We take the high Mg# of the alkali-basalts as indicative of elevated liquidus temperatures and their phenocrysts assemblages as representative of near liquidus phases. The data set of lamprophyres from the Mexican Volcanic Belt is most useful because it constrains a variability of bulk compositions with amphibole and/or biotite phenocrysts including both very potassic and sodic types. We then compared this compiled dataset to the compositions of 13 high Mg# (>60) basaltic to andesitic dikes from the Dariv Igneous Complex. The primitive compositions used in the LLD modeling are included in this set, but not all of these dikes are primitive, but rather, were only selected by the elevated Mg# criterion. Three of these dikes contain biotite as phenocrysts or groundmass phase, seven contain amphibole as a groundmass phase or phenocrysts, and three contain biotite and amphibole in the groundmass.

For biotite, the dominant control on early crystallization is the major element composition, in particular $K_2O$, $TiO_2$, and $Al_2O_3$, of the melt. As to be expected, a high $K_2O$ content and $K_2O/Na_2O$ are critical in determining whether biotite will crystallize near the liquidus (Edgar and Arima, 1983). Biotites have K>>Na while igneous amphiboles have Na>K at crustal pressures. Consequently, higher K/(K+Na) values in a melt will favor biotite crystallization at higher temperatures. Expanding upon an early experimental compilation on high-K starting materials of Edgar and Arima (1983), Figure 8 shows $K_2O$ and $K_2O/Na_2O$ plotted against the difference between the liquidus and biotite crystallization temperatures ($\Delta T_{liq\text{-}bt}$) for various experiments on high-K hydrous basalts at pressures of 0.05-1.0 GPa. With increasing $K_2O$ and $K_2O/Na_2O$, $\Delta T_{liq\text{-}bt}$ decreases at all pressures (Fig. 8a,b). This finding is supported by the fact that high Mg# lamprophyres with relatively high $K_2O/Na_2O$ (> 0.8) have phenocrystic biotite (Fig. 8a). High $TiO_2$ contents also increase the thermal stability of biotite (Edgar and Arima 1983; Righter and

Carmichael 1996), a fact which is reflected in a decrease in $\Delta T_{liq\text{-}bt}$ with increasing $TiO_2$ content (Fig. 8c). High Mg# lamprophyres with elevated $TiO_2$ contents (>1.2 wt.%) generally contain biotite, but not amphibole phenocrysts (Fig. 9c). In contrast, low $Al_2O_3$ concentrations in a melt appear to stabilize biotite (Fig. 8d). In support of this observation, high Mg# lamprophyres and experimental starting materials with biotite as a near liquidus phase tend to have lower $Al_2O_3$ contents (mostly <14 wt.%) than those with amphibole (generally >14 wt.%) (Fig. 9b). It is important to note that in the dataset several of the investigated compositional variables are correlated with each other. For example, $K_2O$ and $TiO_2$ are positively correlated with $K_2O/Na_2O$, whereas $Na_2O$ and $Al_2O_3$ are negatively correlated (see the Electronic Supplementary Material). F has been shown to stabilize biotite to significantly higher temperatures (Foley et al. 1986), however, as the biotites from Dariv do not have particularly high F contents (generally 0.2-0.6 wt.%, Bucholz et al. 2014) we do not explore the effect of this compositional parameter further.

In contrast, the water content of the melt is perhaps the strongest control on the appearance of amphibole. Numerous experimental studies have demonstrated that with increasing $P_{H2O}$ the temperature difference between the liquidus and the onset of amphibole crystallization decreases (Grove et al. 2003; Holloway and Burnham 1972; Krawczynski et al. 2012). Conversely, biotite may crystallize under strongly water-undersaturated conditions. For example, Naney (1983) on a granodioritic melt, found that amphibole crystallized only at relatively high water contents (4 wt.% $H_2O$ at 0.2 GPa and 2.5 wt.% $H_2O$ at 0.8 GPa) whereas biotite crystallized at significantly lower water concentrations (<0.5 wt.% $H_2O$). Further, in water under-saturated andesites at 0.8-1.2 GPa, 4 wt.% $H_2O$ is required to stabilize amphibole at high temperatures (Alonso-Perez et al. 2009). Experimental studies on K-rich basaltic starting compositions have also found biotite as a stable phase under $H_2O$-undersaturated conditions (Barton and Hamilton 1979; Esperança and Holloway 1987). However, as biotite is a hydrous phase, some water is required for its crystallization and at very low pressures and thus low $P_{H_2O}$, biotite is depressed from the liquidus (e.g. at 0.05 GPa, Fig. 8).

Thus, while biotite crystallization strongly depends on the degree of K-enrichment in a melt, amphibole crystallization requires a certain $H_2O$-content. It is important to note that amphibole and biotite are not necessarily in direct 'competition' as crystallizing phases, their relative proximity to the basalt liquidus being controlled in part by different parameters. There is a critical threshold in $K_2O/Na_2O$ and in $TiO_2$ and $Al_2O_3$ contents where near-liquidus biotite crystallization is strongly enhanced, rendering it the primary hydrous high temperature phase. At lower $K_2O/Na_2O$ or $TiO_2$ and higher $Al_2O_3$ contents, amphibole, not biotite, is the stable hydrous phase at high temperatures. $K_2O$-concentration by itself does not lead to such a clear distinction: at >4 wt%, biotite is the near-liquidus hydrous phase, but at lower $K_2O$ contents, low $Al_2O_3$ (< 14 wt.%) and/or high $TiO_2$ (>1.3 wt.%) result in biotite as the high temperature hydrous phase. Surprisingly, CaO concentrations or $Na_2O/CaO$ ratios are of secondary importance within the range of natural magmas (Fig. 9d). $SiO_2$ concentrations are generally (though not

exclusively) lower in the biotite- than amphibole-saturated melts. There is a range within these chemical parameters, i.e. near the thresholds of approximately 14 wt.% $Al_2O_3$, a $K_2O/Na_2O$ of 0.7-0.9, increasing with Si-content, or 1.3 wt.% $TiO_2$, where the melt is compositionally appropriate for both early biotite and amphibole crystallization (Fig. 9). The few phenocrystic amphibole+biotite MVB lamprophyres and one experimental starting material characterized by high temperature crystallization of both amphibole and biotite fall in this range. Also, the high Mg#, biotite±amphibole-bearing dikes from Dariv are situated near these thresholds. As the Dariv high Mg# melt compositions are compositionally suitable for early biotite and amphibole crystallization, it is likely that the $H_2O$-concentrations of the Dariv primitive melts were critical in controlling whether biotite or amphibole crystallized close to the liquidus. Higher concentrations enhance while lower concentrations depress the amphibole crystallization temperature leading to biotite as the high temperature hydrous phase.

In Dariv, amphibole-crystallization occurs in the amphibole-dominated crystallization at much higher temperatures (i.e., in the ultramafic amphibole clinopyroxenites) than in the biotite-dominated sequence, where amphibole only appears in the monzodiorites and more evolved lithologies. Temperatures calculated from clinopyroxene or amphibole-plagioclase thermometry for the amphibole clinopyroxenites and biotite monzodiorites are 1102-1165ºC and 693-726ºC, respectively (Bucholz et al. 2014). We note that the temperature estimates for the amphibole clinopyroxenites are at or above the experimentally established thermal stability of amphibole in hydrous basalts (~1050ºC) (Grove et al. 2003; Krawczynski et al. 2012). This is likely due to errors associated with the clinopyroxene-only thermometer (±50ºC), which would bring the estimates into accord with amphibole crystallization at 1050-1100ºC. Clearly, the ultramafic amphibole clinopyroxenites crystallized at high temperatures suggesting that the melts crystallizing these cumulates had higher water contents than the parental melts of the biotite-dominated sequence. The high Mg# of amphibole (81.0-82.8) and clinopyroxene (84.4-86.2) in the most primitive amphibole clinopyroxenite (MO-10-398) suggest that when the fractionating melt reached Mg#'s of 57-59, $H_2O$-contents were ≥4 wt.% in the amphibole-dominated fractionation series. Using mineral-melt Fe-Mg equilibrium partitioning constraints, we calculate that the parental melts of the amphibole-dominated sequence crystallized ~10-11% clinopyroxene and olivine by mass to reach an Mg# of ~58. This requires that the parental melts of the amphibole-dominated sequence must have had ≥3.5-3.6 wt.% $H_2O$ to reach 4 wt.% $H_2O$ (the minimum amount of $H_2O$ required for amphibole saturation) at a Mg# of 58. In contrast, using mass balance and constraints on the $H_2O$ content required for amphibole crystallization, Bucholz et al. (2014) calculated that the parental melt of the biotite-dominated sequence would contain 2.2-2.6 wt.% $H_2O$ in order to saturate in amphibole when the fractionating melt reached a monzodioritic composition.

*Effects of Biotite versus Amphibole Crystallization on the Geochemistry of Fractionating Arc-Related Melts*

The Dariv alkaline arc series allows for the reconstruction of a LLD dominated by biotite fractionation. Amphibole fractionation has been previously well documented in the field and in experiments and is thought to constitute the dominant mechanism for generating the geochemical trends of calc-alkaline magmatic sequences (Cawthorn and O'Hara 1976; Dessimoz et al. 2012; Grove et al. 2003; Jagoutz 2010; Sisson and Grove 1993). As such, we are able to discuss the effect of biotite versus amphibole crystallization on the geochemistry of a fractionating primitive arc melt by comparing the high-K LLD modeled here with that ascertained for the calc-alkaline series.

Crystallization of biotite vs. amphibole each result in some key trends observed in arc magmatic sequences. First, as $TiO_2$ is compatible and $SiO_2$ contents are low in both minerals, their fractionation is able to produce the characteristic decrease in $TiO_2$ with increasing $SiO_2$ in arc related plutonic and volcanic rocks. Conversely, amphibole and biotite crystallization will result in distinctly different trends in terms of Na and K. This is most clearly seen in the $K_2O/Na_2O$ ratio of the cumulates and evolving melts. The biotite ultramafic cumulates from Dariv reach 4.5 wt.% $K_2O$, depending on the mode of biotite. Conversely, $Na_2O$ contents are <0.8 wt.% resulting in $K_2O/Na_2O$ > 1.4 for the ultramafic phlogopite cumulates. $K_2O/Na_2O$ ratios of the mafic biotite cumulates decrease to ~1, due to the crystallization of oligoclase to andesine. Importantly, K-feldspar co-crystallizes with plagioclase ($An_{13}$-$An_{40}$) resulting in bulk $K_2O/Na_2O$ ratios that do not decrease much further in the biotite-series. In contrast, hornblendites and hornblende gabbros from paleo-arc fractionation sequences have significantly higher $Na_2O$ (typically 1.7-2.2 wt.%) whereas their $K_2O$ content is almost at trace levels leading to $K_2O/Na_2O$ ratios of <0.2 in bulk cumulates (Jagoutz, 2010). Consequently, biotite and K-feldspar crystallization will serve to moderate $K_2O/Na_2O$ ratios in crystallizing melts that initially have $K_2O/Na_2O$ of 1-2, whereas amphibole crystallization will increase this ratio in calc-alkaline series. The resulting convergence of $K_2O/Na_2O$ ratios with fractionation is exemplified by comparing the Dariv high-K LLD to that of a modeled calc-alkaline LLD for the Kohistan paleo-island arc (Fig. 10). The primitive melts identified for the Dariv Igneous Complex have $K_2O/ Na_2O$ ratios of 0.74-1.15. The modeled LLD does not deviate from this range of values, varying between 0.94-1.18 from 52-74 wt.% $SiO_2$. In contrast, the primitive melt identified for the Kohistan paleo-arc has a relatively low $K_2O/Na_2O$ ratio (~0.25), but the modeled LLD results in a strong increase of this value with increasing $SiO_2$ content (to 0.76 at 69 wt.% $SiO_2$). Comparison to a compilation of arc-related granitoids from the Sierra Nevada, S. California, and the Peninsular Range Batholith reinforces these distinct trends resulting from biotite versus amphibole fractionation (Fig. 10). High-K or monzonitic granitoids generally have high $K_2O/Na_2O$ (>0.6) values across a wide array of $SiO_2$ contents (50-75 wt.%) and are in good agreement with the Dariv high-K LLD. Conversely, calc-alkaline granitoids show a general trend of increasing $K_2O/Na_2O$ with increasing $SiO_2$ content, indicative of fractionation of low $K_2O/Na_2O$ cumulates, such as in magmatic hornblendites. Nevertheless, absolute $K_2O$, and consequently $K_2O+Na_2O$ contents, are higher in the biotite-dominated monzonitic series than the calc-alkaline series (Fig. 3c,d).

Though not as distinct, trends similar to $K_2O$ are observed for trace elements compatible in biotite, such as Rb and Ba. In the Dariv high-K LLD, these have high concentrations in the primitive melt, but because of their compatibility in biotite and also K-feldspar, their enrichment during fractionation is moderated with increasing $SiO_2$. As these elements are incompatible in amphibole (and other typical fractionating minerals in the calc-alkaline sequence), these elements show a distinct enrichment with increasing $SiO_2$ in the calc-alkaline LLD and granitoids. Another interesting feature is the general high levels of Sr in monzonitic series relative to the calc-alkaline series. Although both series generally display Sr depletion with increasing $SiO_2$ due to feldspar fractionation, the monzonitic trend is offset several hundred ppm higher from the calc-alkaline trend (Fig. 3f). This is mostly due to the elevated initial Sr concentrations in the primitive high-K basalts consistent with higher levels of addition of an also K-, Rb-, and Ba-rich subduction component.

*Implications for the Mantle Wedge and Subduction Component*

The amphibole- and biotite-series arise from two contrasting primary magma compositions. The normal calc-alkaline, amphibole series has a relatively sodic and $H_2O$-rich primitive melt as a parental magma, while the biotite-series has a comparatively more potassic and LILE-rich, but less hydrous parental melt. Apparently, LILE (including K) and $H_2O$ in the subduction component are decoupled for these two series and we envision two different scenarios for the generation of their parental melts in the mantle wedge.

For the the calc-alkaline amphibole series, the addition of a sodic subduction component concomitant with mantle wedge melting leads to common hydrous sodic primitive arc basalts as, for example, compiled in Jagoutz and Schmidt (2013). In this scenario, the subduction component is likely to be dominated by fluids (Stolper & Newman, 1994; Grove et al. 2002), but may also include a minor sediment melt component which is sodic at moderate pressures (to 3 GPa) and relatively hydrous slab melting conditions (Hermann and Spandler 2008).

For the high-K, biotite series, the subduction signature is increased, but the concentration of $H_2O$ is decreased, leading to two possible scenarios. In the first scenario, one may decouple K+LILE from $H_2O$ by an intermittent stage of crystallization in the mantle wedge. Phlogopite (<1200 $^oC$) and possibly also amphibole (at <1050-1100 $^oC$) could form in a mantle wedge with a temperature colder than that characteristic for primitive arc melts (1250-1350 $^oC$, from multiple saturation experiments, Kushiro 1986, Tatsumi et al. 1994), leading to a sequestration of LILE in these phases, but to further ascent of remnant $H_2O$ through the wedge. Upon heating and/or further fluid-input, this enriched mantle wedge may then deliver a potassic LILE-rich, moderately hydrous primitive arc melt. The first stage may occur when changes in subduction geometry lead to a relatively cooler mantle wedge, most likely causing a hiatus in arc magmatism. In principal, the first stage could also happen in the colder forearc of an active subduction

zone, but more potassic magmatism is characteristic for the main or back arc regions (Kuno, 1965; Dickinson 1975), rendering biotite crystallization in the forearc mantle unlikely.

In the second scenario, a subduction component with a higher (K+LILE)/$H_2O$ ratio than characteristic for normal calc-alkaline magmatism is required. A much less hydrous subduction signal results from slab melts instead of fluids. With increasing pressure sediment melts become highly potassic, particularly when little fluid is available for slab melting (Schmidt et al. 2004). In this scenario, the slab component addition and mantle wedge melting would occur concomitantly, but in contrast to normal calc-alkaline magmas, the slab-component would be dominated by deep (≥3.5 GPa) sediment melts.

For the Dariv Igneous Complex, neither the paleo-geometry of the slab nor the relative time difference between the biotite- and amphibole-series are well-constrained, hence we cannot distinguish which of the above scenarios lead to the spatially overlapping occurrence of the two series. In several modern arcs, potassic volcanism occurs towards the back-arc concomitantly with typical calc-alkaline volcanism in the main arc (e.g., Sunda, Sumatra, Wheller et al. 1987) favoring the second scenario. However, high-K, biotite-phenocrystic basalts in the Sierra Nevada and the Western Mexican Volcanic Belt have been suggested to have formed through a secondary melting event of a previously metasomatized mantle based on their occurrence after subduction had ceased and/or low trace element ratios (e.g., B/Be) indicating little direct input of slab-derived fluids into their source region (Hochstaedter et al. 1996; Ducea and Saleeby, 1998; Farmer et al., 2002). Thus, both scenarios presented above may occur in arcs, depending on the specific geodynamic setting of a particular subduction zone.

***Comparison of Hydrous Basalt LLDs to Quartz-Albite-Orthoclase Ternary Phase Relationships***

The fractionation paths leading to evolved granitic melts both for the high-K and calc-alkaline LLDs are well illustrated in the melting diagram of the system Quartz-Albite-Orthoclase-$H_2O$ (Qz-Ab-Or-$H_2O$, Fig. 11). This ternary system is well constrained over a range of pressures (0.05-1.0 GPa) and from dry to water-saturated conditions (Ebadi and Johannes 1991; Holtz et al. 1989; Luth et al. 1964; Tuttle and Bowen 1958). Notably, the Or/(Ab+Or) ratio of the minimum or eutectic melt increases markedly with decreasing water activity, whereas the normative Qz content remains almost invariant. Conversely, with increasing pressure normative Qz decreases dramatically.

Figure 11 shows CIPW normative compositions of feldspar-bearing lithologies of the Dariv alkaline fractionation sequence plotted onto the Qz-Ab-Or ternary. The monzogabbros, monzodiorites, and several of the monzonites plot just slightly into the silica-undersaturated side of the Ab-Or join. The modeled LLD is also plotted and follows the water-undersaturated ($a_{H_2O}$ = 0.4-0.5) Ab-Or cotectic toward $SiO_2$-enrichment. A few monzonites and late stage felsic dikes fall along this cotectic suggesting that they are representative of liquid compositions. The LLD ultimately ends at the minimum/eutectic at 0.2-0.5 GPa where the majority of the late-stage granitic dikes plot. A pressure range of 0.2-0.5 GPa is in good agreement with intrusion pressures of the Dariv Igneous Complex (Bucholz et al. 2014). Alkali-rich

granitoids from the upper crust of preserved arcs have compositions similar to the calculated LLD. For example, the feldspar-bearing lithologies and LLD of the Dariv alkaline sequence overlaps remarkably well with the compilation of California monzonites of Miller (1977) (Fig. 11b). Instead, amphibole-dominated fractionation sequences lie along the water-saturated cotectic, further supporting our conclusion that the amphibole-dominated fractionation sequence was characterized by higher $H_2O$ contents. For comparison, we also show a compilation of calc-alkaline granitoids from the Sierra Nevada and the modeled calc-alkaline LLD for the Kohistan paleo-arc (Fig. 11b). In contrast to the Dariv LLD, the calc-alkaline granitoids and LLD follow a water-saturated trend towards the eutectic composition. In the Qz-Ab-Or ternary, the relationship of water content and amphibole versus biotite crystallization is directly visible: the calc-alkaline trends are near water-saturated and correspond to amphibole-dominated fractional crystallization, whereas those for the high-K LLD correspond to low water contents and are produced through biotite-dominated crystallization.

**Conclusion**

In contrast to the well-studied liquid lines of descent of calc-alkaline and tholeiitic primitive melts, high-K LLDs have received little attention, perhaps due to the lack of field exposure documenting the cumulative counterpart to the evolving liquids. We present such a LLD based on actual cumulate compositions for the newly discovered alkaline Dariv Igneous Complex in Western Mongolia. We demonstrate that relatively low pressure (0.2-0.4 GPa), hydrous, but not water-saturated fractionation of a primitive alkaline arc magma produces a K-rich monzonitic granitoids series. Critically, fractionation of silica-poor biotite is required to derive such liquids. Although the biotite-dominated ultramafic and mafic cumulates are dominant in the Dariv Igneous Complex, there is a volumetrically subordinate second sequence characterized by early appearance of amphibole. The high temperature appearance of amphibole in this second sequence necessitates higher $H_2O$ contents in its parental melt as compared to the biotite-dominated sequence. Biotite crystallization will moderate enrichments of $K_2O$ and other LILEs with increasing $SiO_2$. These differences result in distinct geochemical signatures for a high-K LLD dominated by biotite crystallization versus a sequence controlled by amphibole fractionation, such as the common calc-alkaline magmatic series.

Although calc-alkaline plutons dominate batholiths in volcanic arcs, high-K granitoids are observed in many continental arcs. These high-K granitoids may critically contribute to the incompatible element budget of continental arcs and hence the bulk continental crust. Hypotheses on the origin of these high-K alkaline granitoids are numerous and include melting of a subducted alkali-rich quartz eclogite (Miller 1977; Miller 1978), partial melting of a garnet-bearing lower crust (Rapela and Pankhurst 1996), and melting of an enriched mantle (Sylvester et al. 1978). Here we document the generation of high-K granitoids through biotite- and clinopyroxene-dominated fractional crystallization of a primitive, alkali-enriched melt. The global spatial and temporal distribution of these high-K suites in relationship to calc-

alkaline arc magmatism, however, has not been cohesively studied and remains essential to fully understand the magmatic and geochemical evolution of volcanic arcs.

**Acknowledgements**

We acknowledge Lydia Zehnder for help with whole rock XRF analyses, Markus Wälle for LA-ICPMS support, Uyanga Bold and Lkhagva-Ochir Said for helping to organize fieldwork logistics, and Adam Bockelie, Yerenburged Munkhbold, and Eson Erdene for their assistance in the field. Reviews by Cin-Ty Lee and an anonymous reviewer helped to clarify ideas presented in this manuscript and are gratefully appreciated.

## References:


Alonso-Perez R, Müntener O, Ulmer P (2009) Igneous garnet and amphibole fractionation in the roots of island arcs: experimental constraints on H2O undersaturated andesitic liquids. Contributions to Mineralogy and Petrology 157:541-558

Annen C, Blundy JD, Sparks RSJ (2006) The Genesis of Intermediate and Silicic Magmas in Deep Crustal Hot Zones. Journal of Petrology 47(3):505-539

Arai S (1994) Characterization of spinel peridotites by olivine-spinel compositional relationships: review and interpretation. Chemical Geology 113(3):191-204

Badarch G, Dickson Cunningham W, Windley BF (2002) A new terrane subdivision for Mongolia: implications for the Phanerozoic crustal growth of Central Asia. Journal of Asian Earth Sciences 21(1):87-110

Barclay J, Carmichael I (2004) A hornblende basalt from western Mexico: water-saturated phase relations constrain a pressure‚Äìtemperature window of eruptibility. Journal of Petrology 45(3):485-506

Barth AP, Wooden JL (2006) Timing of magmatism following initial convergence at a passive margin, southwestern US Cordillera, and ages of lower crustal magma sources. The Journal of Geology 114(2):231-245

Barth MG, McDonough WF, Rudnick RL (2000) Tracking the budget of Nb and Ta in the continental crust. Chemical Geology 165(3):197-213

Barton M, Hamilton D (1978) Water-saturated melting relations to 5 kilobars of three Leucite Hills lavas. Contributions to Mineralogy and Petrology 66(1):41-49

Barton M, Hamilton DL (1979) The melting relationships of a madupite from the Leucite Hills, Wyoming, to 30 Kb. Contributions to Mineralogy and Petrology 69(2):133-142

Bateman PC (1961) Granitic formations in the east-central Sierra Nevada near Bishop, California. Geological Society of America Bulletin 72(10):1521-1537

Blatter DL, Sisson TW, Hankins WB (2013) Crystallization of oxidized, moderately hydrous arc basalt at mid-to lower-crustal pressures: implications for andesite genesis. Contributions to Mineralogy and Petrology 166(3):861-886

Blundy J, Cashman K (2001) Ascent-driven crystallisation of dacite magmas at Mount St Helens, 1980-1986. Contributions to Mineralogy and Petrology 140(6):631-650

Brantley S, Chesley J, Stillings L (1998) Isotopic ratios and release rates of strontium measured from weathering feldspars. Geochimica et Cosmochimica Acta 62(9):1493-1500

Brown G, Thorpe R, Webb P (1984) The geochemical characteristics of granitoids in contrasting arcs and comments on magma sources. Journal of the Geological Society 141(3):413-426

Bucholz CE, Jagoutz O, Schmidt MW, Sambuu O (2014) Phlogopite-and clinopyroxene-dominated fractional crystallization of an alkaline primitive melt: petrology and mineral chemistry of the Dariv Igneous Complex, Western Mongolia. Contributions to Mineralogy and Petrology 167(4):1-28

Buhlmann AL, Cavell P, Burwash RA, Creaser RA, Luth RW (2000) Minette bodies and cognate mica-clinopyroxenite xenoliths from the Milk River area, southern Alberta: records of a complex history of the northernmost part of the Archean Wyoming craton. Canadian Journal of Earth Sciences 37(11):1629-1650

Buslov MM, Saphonova IY, Watanabe T, Obut OT, Fujiwara Y, Iwata K, Semakov NN, Sugai Y, Smirnova LV, Kazansky AY (2001) Evolution of the Paleo-Asian Ocean (Altai-Sayan Region, Central Asia) and collisions of

possible Gondwana-derived terranes with the southern marginal part of the Siberian continent. Geoscience Journal 5(3):203-224

Cawthorn RG, O'Hara M (1976) Amphibole fractionation in calc-alkaline magma genesis. American Journal of Science 276(3):309-329

DeBari SM, Greene AR (2011) Vertical stratification of composition, density, and inferred magmatic processes in exposed arc crustal sections. In: Arc-continent collision, vol. Springer, pp 121-144

Dessimoz M, Müntener O, Ulmer P (2012) A case for hornblende dominated fractionation of arc magmas: the Chelan Complex (Washington Cascades). Contributions to Mineralogy and Petrology 163(4):567-589

Di Carlo I, Pichavant M, Rotolo SG, Scaillet B (2006) Experimental crystallization of a high-K arc basalt: the golden pumice, Stromboli volcano (Italy). Journal of Petrology 47(7):1317-1343

Dickinson WR (1975) Potash-Depth (K-h) Relations in Continental Margin and Intra-Oceanic Magmatic Arcs. Geol 3:53.

Dijkstra AH, Brouwer FM, Cunningham WD, Buchan C, Badarch G, Mason PRD (2006) Late Neoproterozoic proto-arc ocean crust in the Dariv Range, Western Mongolia: a supra-subduction zone end-member ophiolite. Journal of the Geological Society, London 163:363-373

Downes H, MacDonald R, Upton BGJ, Cox KG, Bodinier J-L, Mason PRD, James D, Hill PG, Hearn BC (2004) Ultramafic Xenoliths from the Bearpaw Mountains, Montana, USA: Evidence for Multiple Metasomatic Events in the Lithospheric Mantle beneath the Wyoming Craton. Journal of Petrology 45(8):1631-1662

Ducea M, Saleeby J (1998) A Case for Delamination of the Deep Batholithic Crust beneath the Sierra Nevada, California. International Geology Review 40:78–93. doi: 10.1080/00206819809465199

Ebadi A, Johannes W (1991) Beginning of melting and composition of first melts in the system Qz-Ab-Or-$H_2O$-$CO_2$. Contributions to Mineralogy and Petrology 106(3):286-295

Edgar A, Arima M (1983) Conditions of phlogopite crystallization in ultrapotassic volcanic rocks. Mineralogical Magazine 47(1):11-19

Elburg M, van Bergen MJ, Foden JD (2004) Subducted upper and lower continental crust contributes to magmatism in the collision sector of the Sunda-Banda arc, Indonesia. Geology 32(1):41-44

Esperança S, Holloway JR (1987) On the origin of some mica-lamprophyres: experimental evidence from a mafic minette. Contributions to Mineralogy and Petrology 95(2):207-216

Foley SF, Taylor WR, Green DH (1986) The effect of fluorine on phase relationships in the system $KAlSiO_4$-$Mg_2SiO_4$-$SiO_2$ at 28 kbar and the solution mechanism of fluorine in silicate melts. Contributions to Mineralogy and Petrology 93(1):46-55

Farmer GL, Glazner AF, Manley CR (2002) Did lithospheric delamination trigger late Cenozoic potassic volcanism in the southern Sierra Nevada, California? Geological Society of America Bulletin 114:754–768.

Fowler M, Henney P (1996) Mixed Caledonian appinite magmas: implications for lamprophyre fractionation and high Ba-Sr granite genesis. Contributions to Mineralogy and Petrology 126(1-2):199-215

Fowler M, Henney P, Darbyshire D, Greenwood P (2001) Petrogenesis of high Ba-Sr granites: the Rogart pluton, Sutherland. Journal of the Geological Society 158(3):521-534

Giannetti B, Luhr JF (1990) Phlogopite-clinopyroxenite nodules from high-K magmas, Roccamonfina Volcano, Italy: evidence for a low-pressure metasomatic origin. Earth and Planetary Science Letters 101:404-424

Green TH, Blundy JD, Adam J, Yaxley GM (2000) SIMS determination of trace element partition coefficients between garnet, clinopyroxene and hydrous basaltic liquids at 2-7.5 GPa and 1080-1200ºC. Lithos 53:165-187

Greene AR, DeBari SM, Kelemen PB, Blusztajn J, Clift PD (2006) A Detailed Geochemical Study of Island Arc Crust: the Talkeetna Arc Section, South-Central Alaska. Journal of Petrology 47(6):1051-1093

Grove T, Parman S, Bowring S, et al. (2002) The role of an H2O-rich fluid component in the generation of primitive basaltic andesites and andesites from the Mt. Shasta region, N California. Contrib Mineral Petrol 142:375–396.

Grove TL, Elkins-Tanton LT, Parman SW, Chatterjee N, Müntener O, Gaetani GA (2003) Fractional crystallization and mantle-melting controls on calc-alkaline differentiation trends. Contributions to Mineralogy and Petrology 145:515-533

Hermann J, Spandler CJ (2008) Sediment Melts at Sub-arc Depths: an Experimental Study. Journal of Petrology 49:717–740.

Hochstaedter AG, Ryan JG, Luhr JF (1996) On B/Be ratios in the Mexican volcanic belt. … et Cosmochimica Acta 60:613–628.

Holloway JR, Burnham CW (1972) Melting relations of basalt with equilibrium water pressure less than total pressure. Journal of Petrology 13(1):1-29

Holtz F, Barbey P, Johannes W, Pichavant M (1989) Composition and temperature at the minimum point in the Qz-Ab-Or system for $H_2O$-undersaturated conditions. Experimental investigation. Terra Cognita 1:271-272

Irvine TN, Baragar WRA (1971) A Guide to the Chemical Classification of the Common Volcanic Rocks. Canadian Journal of Earth Sciences 8(5):523-548

Jagoutz O, Müntener O, Schmidt MW, Burg J-P (2011) The roles of flux- and decompression melting and their respective fractionation lines for continental crust formation: Evidence from the Kohistan arc. Earth and Planetary Science Letters 303(1-2):25-36

Jagoutz O, Schmidt MW (2012) The formation and bulk composition of modern juvenile continental crust: The Kohistan arc. Chemical Geology 298-99:79-96

Jagoutz O, Schmidt MW (2013) The composition of the foundered complement to the continental crust and a re-evaluation of fluxes in arcs. Earth and Planetary Science Letters

Jagoutz OE (2010) Construction of the granitoid crust of an island arc. Part II: a quantitative petrogenetic model. Contributions to Mineralogy and Petrology 160:359-381

Janousek V, Farrow CM, Erban V (2006) Interpretation of whole-rock geochemical data in igneous geochemistry: introducing geochemical data toolkit (GCDkit). J Petrol 47:1255-1259.

Kelemen PB, Hanghoj K, Greene AR (2003) 3.18 - One View of the Geochemistry of Subduction-Related Magmatic Arcs, with an Emphasis on Primitive Andesite and Lower Crust. In: Editors-in-Chief: Heinrich DH, Karl KT (eds) Treatise on Geochemistry, vol. Pergamon, Oxford, pp 1-70

Khain EV, Bibikova EV, Salnikova EB, Kröner A, Gibsher AS, Didenko AN, Degtyarev KE, Fedotova AA (2003) The Palaeo-Asian ocean in the Neoproterozoic and early Palaeozoic: new geochronological data and palaeotectonic reconstructions. Precambrian Research 122:329-358

Kovalenko DV, Mongush, AA, Ageeva, OA, Eenzhin, G. (2014) Sources and Geodynamic Environments of Formation of Vendian-Early Paleozoic Magmatic Complexes in the Daribi Range, Western Mongolia. Petrology 22:389-417.

Kozakov IK, Salnikova EB, Khain EV, Kovach VP, Berezhnaya NG, Yakoleva SZ, Plotkina YV (2002) Early Caledonian Crystalline Rocks of the Lake Zone in Mongolia: Formation History and Tectonic Settings as Deduced from U-Pb and Sm-Nd Datings. Geotectonics 36(2):156-166

Krawczynski MJ, Grove TL, Behrens H (2012) Amphibole stability in primitive arc magmas: effects of temperature, $H_2O$ content, and oxygen fugacity. Contributions to Mineralogy and Petrology 164(2):317-339

Kress VC, Carmichael, ISE (1991) The compressibility of silicate liquids containing $Fe_2O_3$ and the effect of composition, temperature, oxygen fugacity and pressure on their redox states. Contributions to Mineralogy and Petrology 108:82-92.

Kuno H (1966) Lateral variation of basalt magma type across continental margins and island arcs. Bulletin Volcanologique

Kushiro I (1987) A petrological model of the mantle wedge and lower crust in the Japanese island arcs. Physicochemical Principles. Geochem Soc Spec Publ, no. 1, ed. Mysen, BO.

Lackey JS, Valley JW, Chen JH, Stockli DF (2008) Dynamic magma systems, crustal recycling, and alteration in the central Sierra Nevada batholith: The oxygen isotope record. Journal of Petrology 49(7):1397-1426

Lameyre J, Bowden P (1982) Plutonic rock types series: discrimination of various granitoid series and related rocks. Journal of Volcanology and Geothermal Research 14(1):169-186

LaTourrette T, Hervig RL, Holloway JR (1995) Trace element partitioning between amphibole, phlogopite, and basanite melt. Earth and Planetary Science Letters 135:13-30

Le Bas MJ, Le Maitre RW, Streckeisen A, Zanettin B (1986) A Chemical Classification of Volcanic Rocks Based on the Total Alkali-Silica Diagram. Journal of Petrology 27(3):745-750

Lee C-TA, Morton DM, Kistler RW, Baird AK (2007) Petrology and tectonics of Phanerozoic continent formation: from island arcs to accretion and continental arc magmatism. Earth and Planetary Science Letters 263(3):370-387

Lobach-Zhuchenko SB, Rollinson H, Chekulaev VP, Savatenkov VM, Kovalenko AV, Martin H, Guseva NS, Arestova NA (2008) Petrology of a Late Archaean, Highly Potassic, Sanukitoid Pluton from the Baltic Shield: Insights into Late Archaean Mantle Metasomatism. Journal of Petrology 49(3):393-420

Luth WC, Jahns RH, Tuttle OF (1964) The granite system at pressures of 4 to 10 kilobars. Journal of geophysical research 69(4):759-773

Middlemost EAK (1994) Naming materials in the magma/igneous rock system. Earth-Science Reviews 37(3-4):215-224

Miller CF (1977) Early alkalic plutonism in the calc-alkalic batholithic belt of California. Geology 5(11):685-688

Miller CF (1978) Monzonitic plutons, California, and a model for generation of alkali-rich, near silica-saturated magmas. Contributions to Mineralogy and Petrology 67(4):349-355

Müntener O, Kelemen P, Grove T (2001) The role of H2O during crystallization of primitive arc magmas under uppermost mantle conditions and genesis of igneous pyroxenites: an experimental study. Contributions to Mineralogy and Petrology 141(6):643-658

Müntener O, Ulmer P (2006) Experimentally derived high-pressure cumulates from hydrous arc magmas and consequences for the seismic velocity structure of lower arc crust. Geophysical Research Letters 33(21):L21308

Nicholls I, Whitford D (1983) Potassium-rich volcanic rocks of the Muriah complex, Java, Indonesia: products of multiple magma sources? Journal of Volcanology and Geothermal Research 18(1):337-359

Peccerillo A, Taylor SR (1976) Geochemistry of eocene calc-alkaline volcanic rocks from the Kastamonu area, Northern Turkey. Contributions to Mineralogy and Petrology 58(1):63-81

Rapela C, Pankhurst R (1996) Monzonite suites: the innermost Cordilleran plutonism of Patagonia. Transactions of the Royal Society of Edinburgh-Earth Sciences 87(1):193-204

Righter K, Carmichael ISE (1996) Phase equilibria of phlogopite lamprophyres from western Mexico: biotite-liquid equilibria and P-T; estimates for biotite-bearing igneous rocks. Contributions to Mineralogy and Petrology 123(1):1-21

Roberts MP, Clemens JD (1993) Origin of high-potassium, calc-alkaline, I-type granitoids. Geology 21(9):825-828

Rudnick RL, Gao S (2003) The composition of the continental crust. In: Rudnick RL (ed) The Crust : Treatise on Geochemistry, vol. Elsevier, Oxford, pp 1-64

Sato H (1977) Nickel content of basaltic magmas: identification of primary magmas and a measure of the degree of olivine fractionation. Lithos 10(2):113-120

Schmidt MW, Vielzeuf D, Auzanneau E (2004) Melting and dissolution of subducting crust at high pressures: the key role of white mica. Earth and Planetary Science Letters 228:65–84.

Sengör AMC, Natalín BA, Burtman VS (1993) Evolution of the Altaid tectonic collage and Palaeozoic crustal growth in Eurasia. Nature 364:299-307

Sengör AMC, Natalín BA, Burtman VS (1994) Tectonic evolution of Altaides. Russian Geology and Geophysics 35:33-47

Sisson TW, Grove TL (1993) Experimental investigations of the role of $H_2O$ in calc-alkaline differentiation and subduction zone magmatism. Contributions to Mineralogy and Petrology 113:143-166

Sisson TW, Ratajeski K, Hankins WB, Glazner AF (2005) Voluminous granitic magmas from common basaltic sources. Contributions to Mineralogy and Petrology 148:635-661

Stolper E, Newman S (1994) The role of water in the petrogenesis of Mariana trough magmas. Earth and Planetary Science Letters 121:293–325. doi: 10.1016/0012-821X(94)90074-4

Sun S, McDonough WF (1989) Chemical and isotopic systematics of oceanic basalts: implications for mantle composition and processes. Geological Society, London, Special Publications 42(1):313-345

Sylvester AG, Miller CF, Nelson C (1978) Monzonites of the White-Inyo Range, California, and their relation to the calc-alkalic Sierra Nevada batholith. Geological Society of America Bulletin 89(11):1677-1687

Sylvester PJ (1989) Post-collisional alkaline granites. The Journal of Geology:261-280

Tatsumi Y, Sakuyama M, Fukuyama H (1983) Generation of arc basalt magmas and thermal structure of the mantle wedge in subduction zones. Journal of Geophysical Research 88:5815–5825.

Taylor SR, McLennan SM (1985) The Continental Crust: Its Composition and Evolution. Blackwell, Oxford

Tuttle OF, Bowen NL (1958) Origin of Granite in the Light of Experimental Studies in the System $NaAlSi_3O_8$-$KAlSi_3O_8$-$SiO_2$-$H_2O$. Geological Society of America,

Villemant B, Jaffrezic H, Joron J-L, Treuil M (1981) Distribution coefficients of major and trace elements; fractional crystallization in the alkali basalt series of Chaîne des Puys (Massif Central, France). Geochimica et Cosmochimica Acta 45(11):1997-2016

Wheller GE, Varne R, Foden JD, Abbott MJ (1987) Geochemistry of Quaternary volcanism in the Sunda-Banda arc, Indonesia, and three-component genesis of island-arc basaltic magmas. Journal of Volcanology and Geothermal Research 32:137–160.

Wolf MB, Wyllie PJ (1994) Dehydration-melting of amphibolite at 10 kbar: the effects of temperature and time. Contributions to Mineralogy and Petrology 115(4):369-383

FIGURE CAPTIONS

***Fig. 1***: (a) Simplified terrane map of Mongolia. Notably, Mongolia consists of Pre-Cambrian autochthonous terranes surrounded by accreted allochthonous terranes, ophiolites, and island arc-related units to the south and west. The Dariv Range is located at the boundary of the Pre-Cambrian Altai Allochthon and the Lake Terrane and is isolated from neighboring ranges by >25 km wide, mainly tertiary basins. (b) Geological map of the detailed study area in the NW part of the Dariv Range showing relationships between the Lake Terrane (the tholeiitic ophiolite sequence, the mantle section, the alkaline fractionation sequence, and low grade metasediments) and the metamorphic Altai Allochthon. The geologic map is based on own field mapping, interpretation of Landsat images, and previously constructed maps of the area (Dijkstra et al. 2006, Khain et al. 2003). (c) Cross-section through Dariv Range showing the overall structure and relationship between various units. Profile location is indicated in Fig. 1b. Note that most contacts in this profile are intrusive in nature. The only two major faults are within the red (alkali-)granites.

**Fig. 2:** Representative photomicrographs illustrating the ultramafic and mafic lithologies of the two studied fractionation sequences. Photomicrographs in the left column (a-d) are from the biotite-dominated sequence, whereas those in the right column (e-h) are from the amphibole-dominated sequence. Whole rock Mg# (molar $Mg/(Mg+Fe^T)$) are plotted in the upper right corners of the images. All images, except g, were taken in plane-polarized light. g is a backscattered electron image. All thin sections are 100 µm thick. Mineral abbreviations are as in Fig. 4. a) Phlogopite-poor wehrlite (MO-10-394). b) Phlogopite-rich wehrlite (MO-10-392) with increased modal percent of biotite. c) Clinopyroxene phlogopitite (MO-11-10) with abundant and large apatite crystals. d) Biotite monzogabbro (MO-11-12) with biotite, clinopyroxene, and feldspar. e) Clinopyroxenite with amphibole and minor biotite (MO-10-398). f) Amphibole-rich clinopyroxenite with apatite (MO-9-251). g) Amphibole clinopyroxenite with apatite (MO-10-329). h) Amphibole monzogabbro (MO-10-309a).

***Fig. 3***: Whole rock Mg#, major, and trace elements versus $SiO_2$ with results of the LLD model described in the text. All analyses are plotted on an anhydrous basis. The black dashed line marks the calculated LLD. Ticks on LLD indicate the melt composition at 10% intervals of melt remaining. Larger faded symbols indicate average cumulate compositions used in the LLD modeling. Red arrows represent the general trend for the calc-alkaline series based on whole rock data from the Sierra Nevada Batholith (Lackey et al., 2008) and the Kohistan Arc (Jagoutz (2010)). Xenolith data is from Buhlmann *et al*. (2000), Downes *et al.* (2004), and Giannetti and Luhr (1990). (a) Mg#, (b) $Al_2O_3$, (c) $Na_2O + K_2O$ (TAS plot modified for plutonic rocks (Le Bas et al. 1986; Middlemost 1994)) (d) $K_2O$, (e) $TiO_2$, (f) Sr.

***Fig. 4***: Trace element spider diagrams normalized to primitive mantle for the biotite-dominated fractionation sequence, (Sun and McDonough 1989) for (a) wehrlites, (b) phlogopite-poor wehrlites, (c) phlogopite-rich wehrlites, (d) phlogopite clinopyroxenites and phlogopitite, (e) monzogabbros, (f) monzodiorites, (g) (quartz-)monzonites, and (h) late-stage felsic dikes.

***Fig. 5***: Trace element spider diagrams normalized to primitive mantle for the amphibole-dominated fractionation sequence, (Sun and McDonough 1989) for (a) amphibole(±biotite) clinopyroxenites, (b) amphibole monzogabbros, and (c) granitoids divided based on $SiO_2$ content. Shaded gray areas indicate the range in composition for similar lithologies of the biotite-dominated sequence.

***Fig. 6*:** Summary of Mg# constraints on LLD modeling. Central panel shows Mg# versus $SiO_2$ (wt.%) of modeled LLD (dashed line) which is colored according to which lithology is crystallizing. Ticks with increments of 10 adjacent to them represent the mass % crystallized at a given point in the LLD trajectory. Large colored circles are the average bulk compositions of the cumulate lithologies used in the model. "Phl" = phlogopite. The gray area indicates field of analyzed dike compositions from the Dariv Range, which are assumed to mostly represent liquid compositions. However, a few outlier dyke groups from the main trend likely result from crystal accumulation. Adjacent panels show Mg# of olivine (left) and

clinopyroxene (right), in addition to the Mg# of calculated equilibrium melts. Open colored circles are averages (with $2\sigma_{SD}$ error bars) of analyzed Mg# of olivine and clinopyroxene for available samples (data from Bucholz et al., 2014). Error bars are omitted for clinopyroxene calculated melts for clarity, but are equivalent to those shown for measured minerals. Filled symbols are the calculated equilibrium melt Mg#. The equilibrium melt Mg# was calculated assuming a $K_d$(Fe-Mg) of 0.3 for olivine-melt (Roeder & Emslie, 1970) and 0.23 for clinopyroxene-melt (Sisson and Grove (1993)). Two calculated melts are shown, one considering all Fe present as $Fe^{2+}$ and the other assuming that $Fe^{3+}/Fe^{T} = 0.35$. This ratio value is equivalent to an oxygen fugacity of +2.3 ΔQFM at 1200ºC and 3000 bars (Kress & Carmichael, 1991), an intermediate value for the estimated oxygen fugacity of crystallization for the phlogopite ultramafic cumulates (+1.8 to +3.2 ΔQFM; Bucholz et al., 2014). Lower and higher $Fe^{3+}/Fe^{T}$ ratios would shift the calculated melt Mg# to lower and higher values, respectively. A black dashed line is included for clarity to separate the two different melt calculations.

***Fig. 7*:** Trace element spider diagram showing results of LLD modeling compared to "liquid-like" whole rock compositions of the biotite dominated fractionation sequence. "Liquid-like" feldspar-bearing samples were identified by their lack of cumulate signature as described in the text under "Model Description". Elements are normalized to primitive mantle composition (Sun and McDonough 1989). Modeled LLD are shown at 80, 40, 20, and 10% melt mass remaining.

***Fig. 8*:** Difference in temperature between the liquidus and biotite saturation versus various compositional parameters of high-K basaltic experimental starting materials at various pressures. Experimental data is from Barclay and Carmichael (2004), Barton and Hamilton (1978), Esperança and Holloway (1987), Nicholls and Whitford (1983), and Righter and Carmichael (1996). (Barclay and Carmichael 2004; Esperança and Holloway 1987; Nicholls and Whitford 1983; Righter and Carmichael 1996). $T_{liquidus}$ of the experiments vary between 1090-1230ºC. (a) $K_2O$, (b) $K_2O/Na_2O$, (c) $TiO_2$, (d) $Al_2O_3$.

***Fig. 9*:** Geochemistry of high-K basalts and hydrous experiments saturated with biotite and/or amphibole in comparison to the Dariv high-Mg# dike compositions. (a) $K_2O/Na_2O$ v. $SiO_2$ (note that y-axis is a logarithmic scale), (b) $Al_2O_3$ v. $SiO_2$, (c) $TiO_2$ v. $SiO_2$, (d) CaO-NaO-$K_2O$. Mexican Volcanic Belt high Mg# alkali-basalts and lamprophyre data (colored circles) are from Allan and Carmichael (1984), Carmichael et al. (1996), Luhr et al. (1989), Luhr and Carmichael (1985), Maria and Luhr (2008), Ownby et al. (2008), Righter and Rosas-Elguera (2001), Vigouroux et al. (2008), Wallace and Carmichael (1989), and Wallace and Carmichael (1992). Amphibole-saturated experimental data (red crosses) are from Alonso-Perez et al. 2009, Di Carlo et al. 2006, Grove et al. 2003, Müntener et al. 2001, Sisson and Grove 1993, and Sisson et al. 2005. Biotite-saturated experimental data (blue crosses) are from Barton and Hamilton (1978), (1979), Edgar and Arima (1983); Edgar and Condliffe (1978), Edgar et al. (1976), Elkins-Tanton and Grove (2003), Esperança and Holloway (1987), Nicholls and Whitford (1983), and Righter and Carmichael (1996). The biotite- and amphibole-saturated experimental data (purple crosses) are from Barclay and Carmichael (2004) and Sisson et al. (2005).

***Fig. 10*:** Comparison of $K_2O/Na_2O$ with $SiO_2$-enrichment for a high-K versus calc-alkaline LLD and arc-related plutonic rocks ($45 < SiO_2 < 80$ wt.%). Data is from the Sierra Nevada, the Peninsular Range Batholith, Southern California Permo-Triassic intrusion, and GEOROC database (http://georoc.mpch-mainz.gwdg.de/georoc/). High-K versus calc-alkaline designation is defined by the $K_2O$ v. $SiO_2$ classification of Pecerillo and Taylor (1976). Sierra Nevada data is from Lackey et al. (2008) and Bateman (1961) . Peninsular Range Batholith data is from Lee et al. (2007). Southern California Permo-Triassic granitoid data is from Barth and Wooden (2006). Arc-related monzodiorites, monzonites, and quartz-monzonites are from the GEOROC database. Note that y-axis is shown with a logarithmic scale. Probability density function contours are plotted using GCDKit 2.3 (Janousek et al., 2006).

***Fig. 11***: Ternary phase diagram in nepheline-kalsilite-quartz system. Figures are zoomed into the section containing the end members albite-K-feldspar-quartz (Ab-Or-Qz). Phase boundaries are from Ebadi and Johannes (1991), Holtz et al. (1989), (1991), Luth et al. (1964), and Tuttle and Bowen (1958). The position of the minimum/euctectic at different water activities are shown by white, gray, and black circles

for water activities of 0.3, 0.5, and 1.0, respectively. Minimum/eutectic positions are shown for pressures of 0.1, 0.2, 0.5, and 1.0 GPa. (a) Projected whole rock data from the Dariv Igneous Complex in the $SiO_2 \geq$ 60% portion of the Qz-Ne-Ks ternary. Data is projected using calculated CIPW norm compositions (mass %) following the projection scheme of Blundy and Cashman (2001) to account for normative anorthite component. For both the amphibole-dominated and biotite-dominated sequence, monzogabbros mostly have >35 wt.% Qz-Ks-Ne (including Or + Ab recalculated into Qz, Ks, and Ne). Biotite monzodiorites and amphibole sequence granitoids with <60 wt.% $SiO_2$ have 40-52 wt.% and 47-74 wt.% Qz-Ks-Ne, respectively. (Qtz-)monzonites, amphibole sequence granitoids with >60 wt.% $SiO_2$, and late stage felsic dikes have 60-95 wt.% Qz-Ks-Ne. All symbols as in Fig. 3. The primitive melt composition (yellow diamond) used in the LLD model (dashed line) is shown for reference. Bulk cumulate compositions used in LLD model are shown as larger faded symbols. Cotectics at water-saturated conditions at 0.1 and 1.0 GPa are shown as gray lines with arrows. (b) Modeled Dariv high-K LLD and Kohistan paleo-arc calc-alkaline LLD compared to arc-related granitoids in the Qz-Ab-Or ternary. Blue field of California monzonites is from Miller (1977). Red field for calc-alkaline granitoids from the Sierra Nevada is from compilation described in Fig. 10.

**Table 1** Compositions used in LLD model.

| | PARENTAL MELT | | | FRACTIONATED CUMULATE COMPOSITIONS | | | | | | | | | | | | | | | | | |
|---|---|---|---|---|---|---|---|---|---|---|---|---|---|---|---|---|---|---|---|---|---|
| | | | | ***Phlogopite Dunite | | Wehrlite | | Phlogopite-Poor Wehrlite | | Phlogopite-Rich Wehrlite | | Phlogopite-Rich Clinopyroxenite | High Mg# Monzogabbro | | Low Mg# Monzogabbro | | Monzodiorite | | Monzonite | |
| | Model Composition** | Average (N=3)* | 2σ | N=3* | 2σ | N=3* | 2σ | N=7* | 2σ | N=4* | 2σ | N=1* | N=5* | 2σ | N=5* | 2σ | N=4* | 2σ | N=3* | 2σ |
| $SiO_2$ | 52.00 | 51.35 | 3.57 | 42.81 | 1.32 | 52.07 | 0.66 | 48.62 | 2.33 | 46.38 | 1.54 | 44.25 | 50.23 | 3.75 | 51.57 | 2.24 | 54.27 | 2.81 | 61.69 | 5.55 |
| $TiO_2$ | 1.10 | 0.90 | 0.56 | 0.10 | 0.04 | 0.26 | 0.12 | 0.40 | 0.16 | 1.25 | 0.88 | 2.83 | 1.10 | 0.44 | 1.32 | 0.36 | 1.10 | 0.14 | 0.63 | 0.29 |
| $Al_2O_3$ | 12.90 | 14.28 | 1.59 | 1.55 | 0.64 | 1.34 | 0.62 | 2.12 | 1.33 | 5.46 | 1.95 | 8.55 | 15.55 | 4.02 | 17.53 | 2.61 | 16.68 | 1.17 | 17.34 | 2.09 |
| FeO | 7.85 | 7.66 | 1.59 | 8.06 | 1.99 | 5.60 | 1.98 | 10.26 | 2.21 | 9.94 | 2.82 | 10.60 | 8.08 | 0.91 | 8.14 | 1.48 | 7.69 | 1.37 | 4.52 | 1.93 |
| MnO | 0.16 | 0.18 | 0.05 | 0.12 | 0.04 | 0.14 | 0.05 | 0.24 | 0.05 | 0.20 | 0.06 | 0.19 | 0.17 | 0.02 | 0.17 | 0.06 | 0.16 | 0.04 | 0.08 | 0.03 |
| MgO | 11.26 | 10.83 | 2.88 | 45.45 | 1.74 | 19.74 | 1.21 | 21.94 | 5.34 | 20.65 | 4.46 | 16.14 | 9.47 | 1.86 | 5.98 | 1.72 | 4.80 | 1.77 | 2.58 | 1.82 |
| CaO | 8.70 | 9.96 | 1.12 | 1.01 | 0.23 | 20.34 | 1.01 | 15.96 | 4.10 | 13.51 | 3.04 | 11.97 | 8.85 | 1.58 | 8.54 | 1.42 | 7.31 | 2.02 | 3.67 | 2.09 |
| $Na_2O$ | 2.50 | 2.21 | 0.72 | - | - | 0.15 | 0.10 | 0.17 | 0.20 | 0.29 | 0.16 | 0.41 | 2.68 | 0.44 | 3.39 | 0.95 | 3.83 | 0.44 | 4.36 | 0.92 |
| $K_2O$ | 2.96 | 2.21 | 1.14 | 0.52 | 0.17 | 0.07 | 0.06 | 0.10 | 0.16 | 2.09 | 1.13 | 3.52 | 3.25 | 1.58 | 2.73 | 1.14 | 3.57 | 1.46 | 4.82 | 0.12 |
| $P_2O_5$ | 0.49 | 0.40 | 0.39 | 0.06 | 0.02 | 0.02 | 0.01 | 0.02 | 0.01 | 0.05 | 0.13 | 1.43 | 0.56 | 0.28 | 0.60 | 0.22 | 0.59 | 0.14 | 0.30 | 0.21 |
| Cr2O3 | 0.08 | 0.03 | 0.09 | 0.32 | - | 0.28 | 0.18 | 0.16 | 0.22 | 0.19 | 0.06 | 0.11 | 0.06 | 0.07 | 0.03 | 0.04 | 0.02 | 0.01 | 0.01 | 0.01 |
| Total | 100.00 | 100.00 | - | 100.00 | - | 100.00 | - | 100.00 | - | 100.00 | - | 100.00 | 100.00 | - | 100.00 | - | 100.00 | - | 100.00 | - |
| **Mg#** | 71.9 | 71.50 | 9.35 | 91.0 | 2.3 | 86.3 | 4.9 | 79.1 | 4.5 | 78.8 | 2.9 | 73.1 | 67.6 | 3.4 | 56.6 | 3.1 | 52.7 | 4.2 | 50.4 | 12.2 |
| Sc | 24.3 | 25.3 | 6.0 | 4.7 | 1.2 | 47.2 | 12.0 | 51.4 | 19.1 | 44.2 | 17.6 | 40.6 | 22.9 | 2.7 | 20.6 | 5.0 | 18.6 | 7.9 | 7.3 | 6.4 |
| V | 203 | 172 | 58 | 28 | 22 | 85 | 56 | 186 | 122 | 267 | 213 | 558 | 189 | 63 | 189 | 77 | 200 | 86 | 64 | 61 |
| Cr | 579 | 602 | 241 | 2967 | 800 | 1750 | 1139 | 1262 | 653 | 1206 | 384 | 739 | 390 | 451 | 185 | 194 | 151 | 32 | 50 | 59 |
| Ni | 239 | 160 | 127 | 2330 | 81 | 208 | 15 | 355 | 244 | 331 | 233 | 289 | 120 | 116 | 50 | 30 | 53 | 11 | 17 | 29 |
| Zn | 59.0 | 62.8 | 10.7 | 55.7 | 26.1 | 25.0 | 14.4 | 53.3 | 25.2 | 51.2 | 10.5 | 64.0 | 63.1 | 14.1 | 66.9 | 14.5 | 68.1 | 9.6 | 46.8 | 13.5 |
| Rb | 85 | 71 | 25 | 23 | 8 | 2 | 2 | 2 | 4 | 58 | 33 | 152 | 105 | 83 | 84 | 47 | 83 | 41 | 116 | 6 |
| Sr | 889 | 856 | 478 | 36 | 4 | 121 | 13 | 96 | 42 | 137 | 73 | 197 | 1397 | 1199 | 1154 | 786 | 1300 | 287 | 1139 | 419 |
| Y | 18.9 | 21.8 | 8.3 | 1.9 | 1.0 | 6.3 | 4.1 | 12.7 | 10.0 | 10.0 | 2.1 | 30.4 | 23.3 | 11.5 | 23.5 | 8.8 | 22.2 | 6.6 | 14.9 | 3.2 |
| Zr | 120 | 159 | 153 | 7 | 4 | 14 | 15 | 22 | 19 | 24 | 9 | 28 | 102 | 48 | 165 | 186 | 204 | 139 | 293 | 85 |
| Nb | 9.0 | 9.3 | 10.8 | 0.6 | 0.2 | 0.2 | 0.4 | 0.2 | 0.5 | 1.6 | 0.3 | 5.3 | 9.3 | 8.4 | 13.4 | 5.7 | 13.0 | 3.2 | 14.9 | 2.5 |
| Cs | 1.55 | 1.83 | 1.41 | 1.15 | 0.92 | 0.20 | 0.19 | 0.17 | 0.26 | 0.94 | 0.56 | 1.80 | 1.88 | 3.92 | 1.65 | 0.54 | 1.83 | 1.05 | 2.10 | 1.58 |
| Ba | 1125 | 766 | 516 | 197 | 71 | 11 | 14 | 27 | 50 | 1217 | 1227 | 2287 | 1382 | 1060 | 797 | 689 | 1173 | 557 | 1421 | 587 |
| La | 30.7 | 42.4 | 27.4 | 1.7 | 0.7 | 3.4 | 2.6 | 3.5 | 2.4 | 4.2 | 4.3 | 28.2 | 43.8 | 24.6 | 38.5 | 8.7 | 39.7 | 9.1 | 47.1 | 35.8 |
| Ce | 67.0 | 87.7 | 56.6 | 3.7 | 1.9 | 10.5 | 8.0 | 12.1 | 7.7 | 14.4 | 10.8 | 70.8 | 101.9 | 61.0 | 80.5 | 18.4 | 81.9 | 13.4 | 89.6 | 58.8 |
| Pr | 8.2 | 10.3 | 6.7 | - | - | 1.6 | 1.2 | 2.1 | 1.3 | 2.4 | 1.4 | 10.3 | 12.8 | 8.1 | 9.9 | 2.9 | 9.6 | 1.0 | 9.7 | 4.7 |
| Nd | 35.6 | 42.4 | 26.4 | 2.2 | 1.5 | 8.8 | 5.3 | 12.2 | 7.6 | 13.1 | 6.4 | 51.3 | 54.8 | 34.0 | 42.2 | 14.5 | 40.3 | 4.5 | 36.4 | 12.8 |
| Sm | 7.22 | 7.65 | 4.46 | 0.55 | 0.38 | 2.27 | 1.10 | 3.73 | 2.29 | 3.77 | 1.82 | 11.84 | 10.17 | 6.01 | 8.36 | 3.17 | 8.12 | 1.86 | 6.22 | 0.74 |
| Eu | 1.82 | 1.93 | 1.06 | 0.17 | 0.16 | 0.58 | 0.27 | 0.94 | 0.49 | 1.04 | 0.45 | 1.83 | 2.72 | 1.59 | 2.28 | 0.97 | 2.17 | 0.45 | 1.83 | 0.46 |
| Gd | 5.80 | 6.04 | 2.68 | - | - | 1.87 | 1.19 | 3.75 | 2.45 | 3.52 | 0.98 | 9.49 | 7.78 | 4.98 | 6.92 | 2.68 | 6.69 | 1.54 | 4.38 | 0.31 |
| Tb | 0.700 | 0.791 | 0.364 | 0.068 | 0.047 | 0.264 | 0.156 | 0.483 | 0.333 | 0.446 | 0.123 | 1.085 | 0.949 | 0.532 | 0.810 | 0.236 | 0.777 | 0.161 | 0.591 | 0.092 |
| Dy | 3.85 | 4.18 | 1.84 | 0.42 | 0.27 | 1.42 | 1.16 | 2.69 | 1.94 | 2.41 | 0.44 | 6.25 | 4.96 | 2.57 | 4.55 | 1.73 | 4.36 | 0.91 | 3.00 | 0.42 |
| Ho | 0.680 | 0.810 | 0.210 | - | - | 0.262 | 0.236 | 0.488 | 0.346 | 0.378 | 0.049 | 1.139 | 0.847 | 0.483 | 0.863 | 0.325 | 0.785 | 0.222 | 0.500 | 0.084 |
| Er | 1.81 | 2.15 | 0.81 | - | - | 0.53 | 0.62 | 1.27 | 0.87 | 1.00 | 0.38 | 2.92 | 2.23 | 0.98 | 2.37 | 0.86 | 2.08 | 0.71 | 1.44 | 0.33 |
| Tm | 0.230 | 0.282 | 0.177 | - | - | 0.084 | 0.072 | 0.169 | 0.131 | 0.114 | 0.032 | 0.337 | 0.272 | 0.077 | 0.287 | 0.099 | 0.291 | 0.164 | 0.203 | 0.074 |
| Yb | 1.58 | 1.80 | 0.75 | 0.19 | 0.04 | 0.40 | 0.68 | 1.10 | 0.85 | 0.82 | 0.41 | 2.02 | 1.82 | 0.72 | 1.98 | 0.99 | 2.06 | 0.78 | 1.38 | 0.49 |
| Lu | 0.235 | 0.281 | 0.135 | 0.032 | 0.006 | 0.084 | 0.063 | 0.145 | 0.132 | 0.112 | 0.044 | 0.313 | 0.266 | 0.086 | 0.311 | 0.117 | 0.291 | 0.086 | 0.154 | 0.057 |
| Hf | 3.25 | 3.81 | 3.34 | 0.25 | 0.01 | 0.56 | 0.44 | 0.92 | 0.75 | 0.95 | 0.31 | 0.97 | 2.68 | 0.97 | 5.48 | 3.24 | 4.71 | 2.61 | 6.82 | 1.90 |
| Ta | 0.53 | 0.57 | 0.67 | 0.03 | 0.01 | 0.01 | 0.04 | 0.02 | 0.05 | 0.08 | 0.03 | 0.31 | 0.43 | 0.43 | 0.69 | 0.21 | 0.80 | 0.18 | 0.80 | 0.28 |
| Pb | 7.3 | 5.0 | 4.9 | 2.0 | 1.1 | 0.3 | 0.3 | 0.4 | 0.7 | 0.6 | 1.2 | 1.0 | 5.6 | 6.2 | 7.5 | 2.8 | 11.0 | 6.7 | 20.9 | 4.5 |
| Th | 4.0 | 7.6 | 5.3 | 0.6 | 0.2 | 0.3 | 0.4 | 0.2 | 0.5 | 0.2 | 0.4 | 1.0 | 3.3 | 4.4 | 4.2 | 4.9 | 3.4 | 1.8 | 8.9 | 9.1 |
| U | 1.11 | 1.82 | 0.12 | 3.81 | 2.87 | 0.07 | 0.14 | 0.08 | 0.17 | 0.06 | 0.14 | 0.32 | 1.02 | 1.39 | 1.28 | 1.24 | 0.97 | 0.45 | 2.02 | 1.18 |

* N equals the number of samples of a lithology included in average. Analyses recalculated on an anhydrous basis with all Fe calculated as $FeO^t$.
** Composition used in LLD model.
*** Average of WC-232, WC-253, & WC-251 from Downes *et al.* (2004)

**Table 2** Calculated LLD Compositions

| % Melt Remaining | *0.90* | *0.80* | *0.70* | *0.60* | *0.50* | *0.40* | *0.30* | *0.20* | *0.10* |
|---|---|---|---|---|---|---|---|---|---|
| $SiO_2$ | 52.56 | 53.28 | 54.47 | 55.28 | 56.28 | 57.48 | 58.98 | 61.31 | 68.36 |
| $TiO_2$ | 1.18 | 1.20 | 1.03 | 1.00 | 0.98 | 0.90 | 0.80 | 0.64 | 0.19 |
| $Al_2O_3$ | 14.10 | 15.31 | 16.36 | 16.59 | 16.79 | 16.66 | 16.52 | 16.44 | 16.19 |
| FeO | 7.86 | 7.58 | 7.18 | 7.00 | 6.78 | 6.45 | 5.96 | 5.11 | 2.54 |
| MnO | 0.16 | 0.15 | 0.15 | 0.14 | 0.14 | 0.13 | 0.12 | 0.10 | 0.04 |
| MgO | 8.93 | 7.38 | 6.01 | 5.33 | 4.51 | 4.05 | 3.62 | 3.04 | 1.28 |
| CaO | 8.61 | 7.89 | 7.27 | 6.96 | 6.59 | 6.10 | 5.50 | 4.60 | 1.90 |
| $Na_2O$ | 2.76 | 3.08 | 3.45 | 3.62 | 3.80 | 3.92 | 4.02 | 4.11 | 4.39 |
| $K_2O$ | 3.24 | 3.45 | 3.49 | 3.53 | 3.59 | 3.79 | 4.00 | 4.21 | 4.85 |
| $P_2O_5$ | 0.53 | 0.60 | 0.53 | 0.51 | 0.50 | 0.48 | 0.45 | 0.38 | 0.17 |
| Cr2O3 | 0.06 | 0.05 | 0.03 | 0.03 | 0.02 | 0.02 | 0.02 | 0.01 | 0.00 |
| Total | 100 | 100 | 100 | 100 | 100 | 100 | 100 | 100 | 100 |
| **Mg#** | 66.9 | 63.5 | 59.9 | 57.6 | 54.2 | 52.8 | 52.0 | 51.5 | 47.4 |
| Sc | 24.1 | 21.3 | 18.5 | 17.5 | 16.4 | 15.3 | 13.9 | 11.6 | 4.5 |
| V | 217 | 213 | 174 | 168 | 163 | 157 | 144 | 117 | 33 |
| Cr | 399 | 294 | 216 | 181 | 140 | 124 | 109 | 89 | 27 |
| Ni | 124 | 97 | 69 | 58 | 46 | 43 | 40 | 33 | 14 |
| Zn | 60.4 | 61.5 | 61.5 | 61.3 | 60.9 | 59.5 | 56.8 | 51.2 | 34.3 |
| Rb | 93 | 99 | 95 | 92 | 90 | 91 | 93 | 98 | 113 |
| Sr | 975 | 1084 | 1210 | 1191 | 1151 | 1144 | 1113 | 1021 | 741 |
| Y | 20.3 | 21.5 | 21.0 | 20.5 | 19.9 | 19.0 | 17.7 | 15.5 | 8.9 |
| Zr | 131 | 145 | 162 | 173 | 187 | 194 | 197 | 193 | 183 |
| Nb | 9.9 | 11.0 | 11.9 | 12.5 | 13.1 | 13.1 | 13.1 | 13.1 | 13.2 |
| Cs | 1.64 | 1.76 | 1.78 | 1.76 | 1.74 | 1.76 | 1.76 | 1.72 | 1.62 |
| Ba | 1232 | 1274 | 1169 | 1121 | 1070 | 1123 | 1163 | 1158 | 1142 |
| La | 33.7 | 37.5 | 39.6 | 39.0 | 38.1 | 37.8 | 37.4 | 36.3 | 32.9 |
| Ce | 73.3 | 80.9 | 84.3 | 81.5 | 77.5 | 76.2 | 74.5 | 70.8 | 59.8 |
| Pr | 9.0 | 9.9 | 10.1 | 9.6 | 9.0 | 8.7 | 8.4 | 7.7 | 5.9 |
| Nd | 38.7 | 42.0 | 42.0 | 39.9 | 36.9 | 35.3 | 33.3 | 29.8 | 19.3 |
| Sm | 7.81 | 8.33 | 8.11 | 7.73 | 7.25 | 6.93 | 6.49 | 5.68 | 3.24 |
| Eu | 1.97 | 2.09 | 2.15 | 2.06 | 1.93 | 1.84 | 1.71 | 1.47 | 0.77 |
| Gd | 6.28 | 6.62 | 6.43 | 6.17 | 5.85 | 5.56 | 5.15 | 4.39 | 2.09 |
| Tb | 0.752 | 0.790 | 0.771 | 0.738 | 0.696 | 0.665 | 0.622 | 0.545 | 0.312 |
| Dy | 4.14 | 4.35 | 4.21 | 4.06 | 3.89 | 3.71 | 3.46 | 3.02 | 1.67 |
| Ho | 0.734 | 0.776 | 0.751 | 0.730 | 0.707 | 0.669 | 0.618 | 0.535 | 0.284 |
| Er | 1.96 | 2.07 | 2.02 | 1.97 | 1.92 | 1.82 | 1.68 | 1.49 | 0.89 |
| Tm | 0.248 | 0.264 | 0.261 | 0.258 | 0.256 | 0.248 | 0.235 | 0.207 | 0.122 |
| Yb | 1.70 | 1.81 | 1.82 | 1.81 | 1.81 | 1.77 | 1.69 | 1.51 | 0.96 |
| Lu | 0.253 | 0.269 | 0.270 | 0.270 | 0.271 | 0.263 | 0.250 | 0.230 | 0.168 |
| Hf | 3.54 | 3.88 | 4.29 | 4.59 | 4.96 | 4.91 | 4.85 | 4.93 | 5.14 |
| Ta | 0.58 | 0.65 | 0.71 | 0.76 | 0.82 | 0.86 | 0.90 | 0.95 | 1.10 |
| Pb | 7.9 | 8.9 | 10.0 | 10.8 | 11.9 | 13.0 | 14.2 | 15.8 | 20.6 |
| Th | 4.4 | 4.9 | 5.5 | 5.9 | 6.4 | 7.0 | 8.0 | 10.3 | 17.3 |
| U | 1.02 | 1.14 | 1.26 | 1.31 | 1.37 | 1.40 | 1.50 | 1.76 | 2.55 |

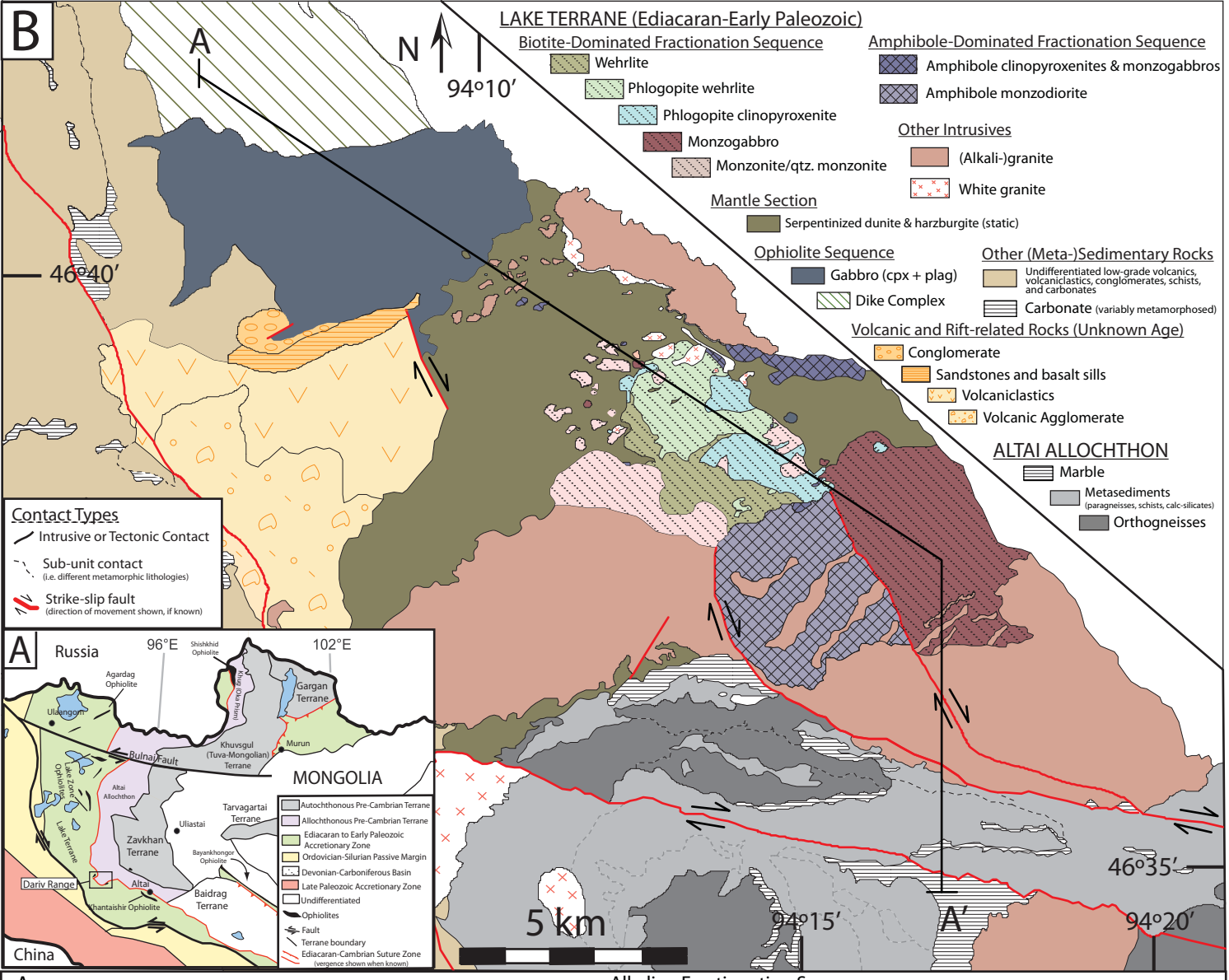
B
A
N
94°10′
46°40′
LAKE TERRANE (Ediacaran-Early Paleozoic)
Biotite-Dominated Fractionation Sequence
Wehrlite
Phlogopite wehrlite
Phlogopite clinopyroxenite
Monzogabbro
Monzonite/qtz. monzonite
Amphibole-Dominated Fractionation Sequence
Amphibole clinopyroxenites & monzogabbros
Amphibole monzodiorite
Other Intrusives
(Alkali-)granite
White granite
Mantle Section
Serpentinized dunite & harzburgite (static)
Ophiolite Sequence
Gabbro (cpx + plag)
Dike Complex
Other (Meta-)Sedimentary Rocks
Undifferentiated low-grade volcanics, volcaniclastics, conglomerates, schists, and carbonates
Carbonate (variably metamorphosed)
Volcanic and Rift-related Rocks (Unknown Age)
Conglomerate
Sandstones and basalt sills
Volcaniclastics
Volcanic Agglomerate
ALTAI ALLOCHTHON
Marble
Metasediments
(paragneisses, schists, calc-silicates)
Orthogneisses
Contact Types
Intrusive or Tectonic Contact
Sub-unit contact
(i.e. different metamorphic lithologies)
Strike-slip fault
(direction of movement shown, if known)
A
Russia
96°E
102°E
Shishkhid Ophiolite
Agardag Ophiolite
Ulaangom
Gargan Terrane
Khuvsgul (Tuva-Mongolian) Terrane
Murun
Bulnay Fault
MONGOLIA
Altai Allochthon
Tarvagartai Terrane
Uliastai
Zavkhan Terrane
Bayankhongor Ophiolite
Dariv Range
Altai
Baidrag Terrane
Khantaishir Ophiolite
China
Autochthonous Pre-Cambrian Terrane
Allochthonous Pre-Cambrian Terrane
Ediacaran to Early Paleozoic Accretionary Zone
Ordovician-Silurian Passive Margin
Devonian-Carboniferous Basin
Late Paleozoic Accretionary Zone
Undifferentiated
Ophiolites
Fault
Terrane boundary
Ediacaran-Cambrian Suture Zone
(vergence shown when known)
5 km
94°15′
A′
46°35′
94°20′
A
Ophiolite Sequence
Mantle
Alkaline Fractionation Sequence
A′
Dike Complex
Transition Zone
Gabbro
Plagiogranite Dike
(Alkali-)Granite Intrusions
Serpentinized Harzburgite
Hbl. Gabbro
(Qtz.)-Monzonite
Phlogopite Wehrlite
Phlogopite Clinopyroxenite
Monzogabbro
Felsic Dike
Alkali-basalt Dike
(Alkali-)Granite
Metasediments of the Altai Allochthon
Dunite Dikes
Elevation (m)
2400
2200
2000
1800
1600
5
10
15
20
Horizontal Distance (km)
C

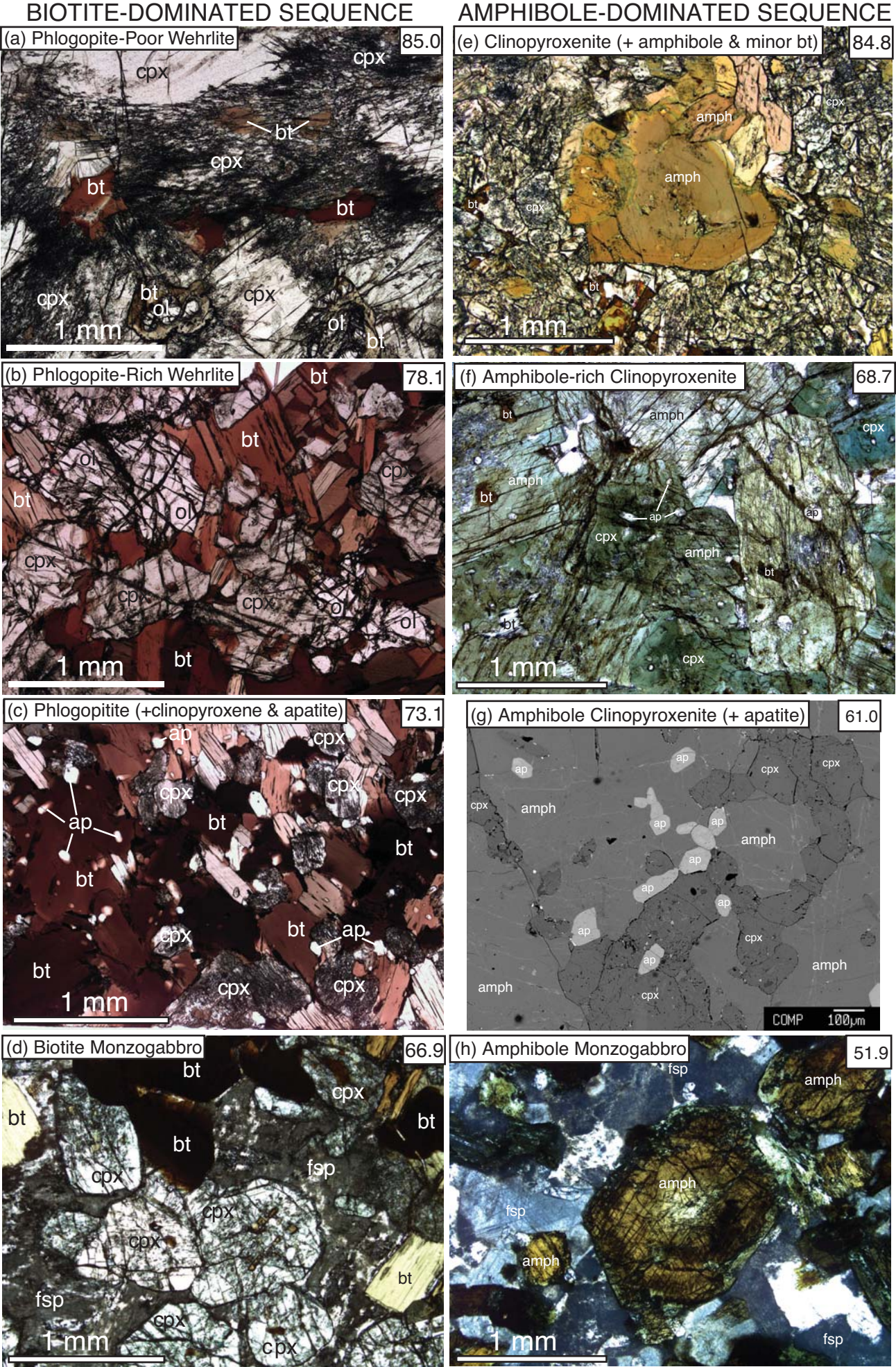
BIOTITE-DOMINATED SEQUENCE
AMPHIBOLE-DOMINATED SEQUENCE
(a) Phlogopite-Poor Wehrlite
85.0
(b) Phlogopite-Rich Wehrlite
78.1
(c) Phlogopitite (+clinopyroxene & apatite)
73.1
(d) Biotite Monzogabbro
66.9
(e) Clinopyroxenite (+ amphibole & minor bt)
84.8
(f) Amphibole-rich Clinopyroxenite
68.7
(g) Amphibole Clinopyroxenite (+ apatite)
61.0
(h) Amphibole Monzogabbro
51.9
1 mm
COMP 100µm

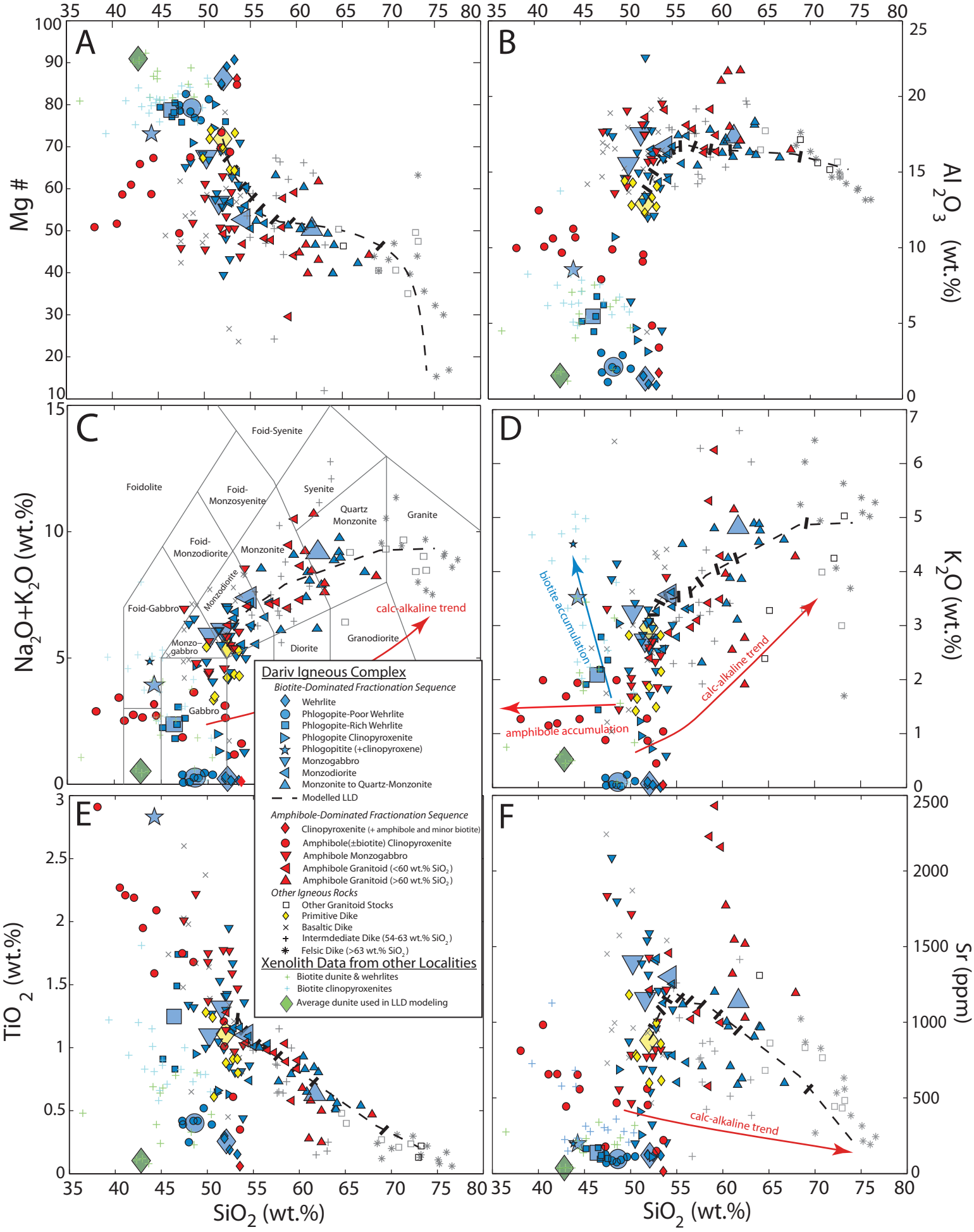
A
B
C
D
E
F
Mg #
Al2O3 (wt.%)
Na2O+K2O (wt.%)
K2O (wt.%)
TiO2 (wt.%)
Sr (ppm)
SiO2 (wt.%)
SiO2 (wt.%)
Foidolite
Foid-Syenite
Foid-Monzosyenite
Syenite
Quartz Monzonite
Granite
Foid-Monzodiorite
Monzonite
Monzodiorite
Foid-Gabbro
Monzo-gabbro
Diorite
Granodiorite
Gabbro
calc-alkaline trend
biotite accumulation
amphibole accumulation
Dariv Igneous Complex
Biotite-Dominated Fractionation Sequence
Wehrlite
Phlogopite-Poor Wehrlite
Phlogopite-Rich Wehrlite
Phlogopite Clinopyroxenite
Phlogopitite (+clinopyroxene)
Monzogabbro
Monzodiorite
Monzonite to Quartz-Monzonite
Modelled LLD
Amphibole-Dominated Fractionation Sequence
Clinopyroxenite (+ amphibole and minor biotite)
Amphibole(±biotite) Clinopyroxenite
Amphibole Monzogabbro
Amphibole Granitoid (<60 wt.% SiO2)
Amphibole Granitoid (>60 wt.% SiO2)
Other Igneous Rocks
Other Granitoid Stocks
Primitive Dike
Basaltic Dike
Intermdediate Dike (54-63 wt.% SiO2)
Felsic Dike (>63 wt.% SiO2)
Xenolith Data from other Localities
Biotite dunite & wehrlites
Biotite clinopyroxenites
Average dunite used in LLD modeling

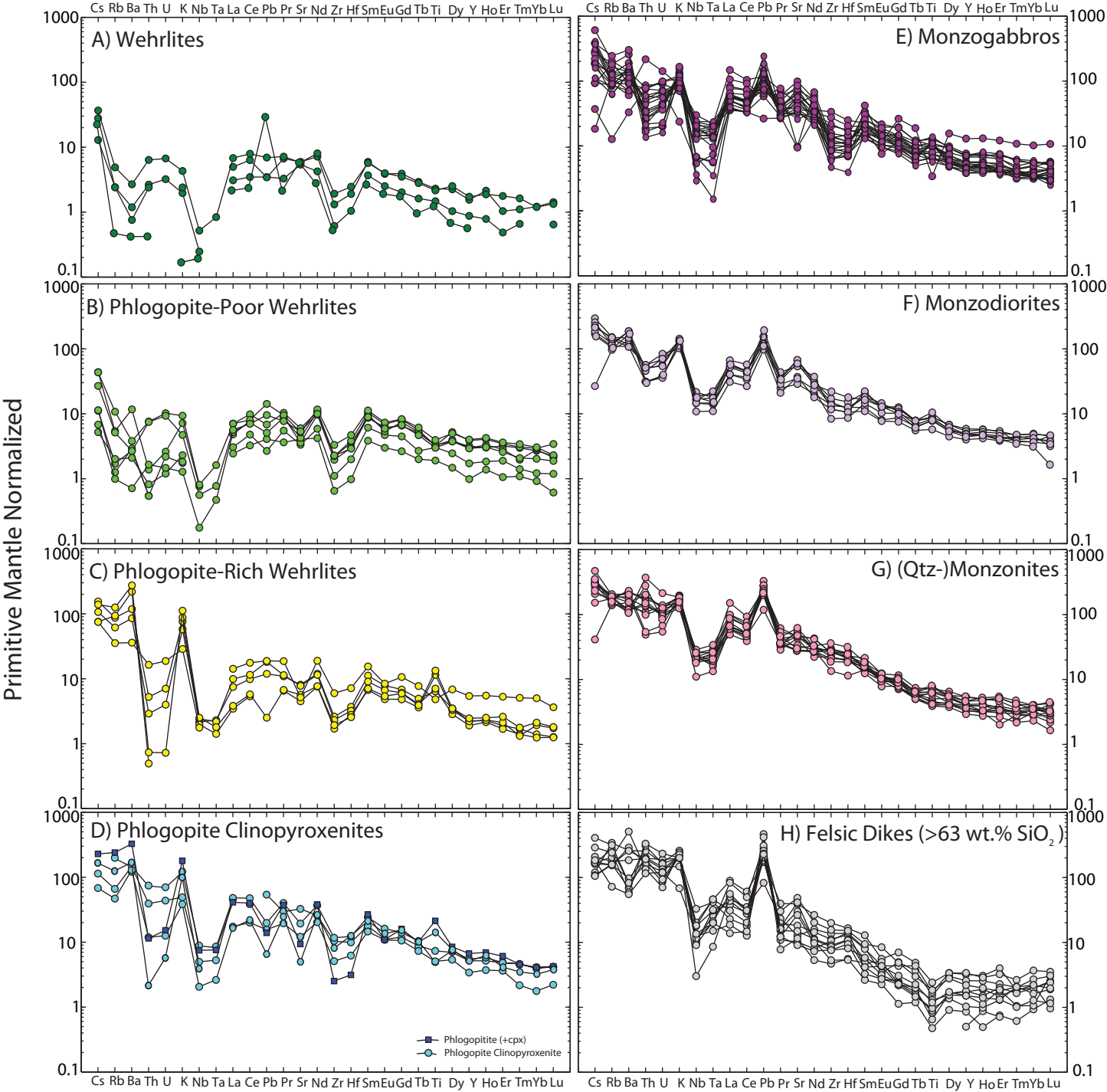
A) Wehrlites
B) Phlogopite-Poor Wehrlites
C) Phlogopite-Rich Wehrlites
D) Phlogopite Clinopyroxenites
E) Monzogabbros
F) Monzodiorites
G) (Qtz-)Monzonites
H) Felsic Dikes (>63 wt.% SiO2)
Primitive Mantle Normalized
Cs Rb Ba Th U K Nb Ta La Ce Pb Pr Sr Nd Zr Hf Sm Eu Gd Tb Ti Dy Y Ho Er Tm Yb Lu
1000
100
10
1
0.1
Phlogopitite (+cpx)
Phlogopite Clinopyroxenite

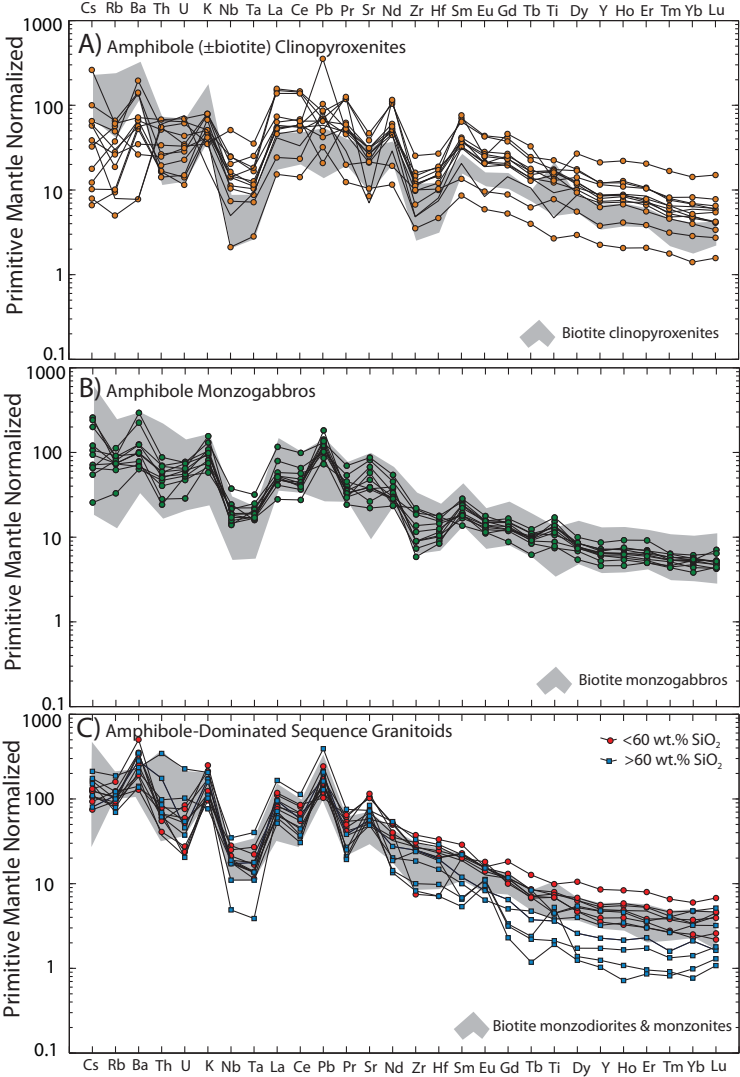
Cs Rb Ba Th U K Nb Ta La Ce Pb Pr Sr Nd Zr Hf Sm Eu Gd Tb Ti Dy Y Ho Er Tm Yb Lu
Primitive Mantle Normalized
1000
100
10
1
0.1
A) Amphibole (±biotite) Clinopyroxenites
Biotite clinopyroxenites
B) Amphibole Monzogabbros
Biotite monzogabbros
C) Amphibole-Dominated Sequence Granitoids
<60 wt.% SiO2
>60 wt.% SiO2
Biotite monzodiorites & monzonites

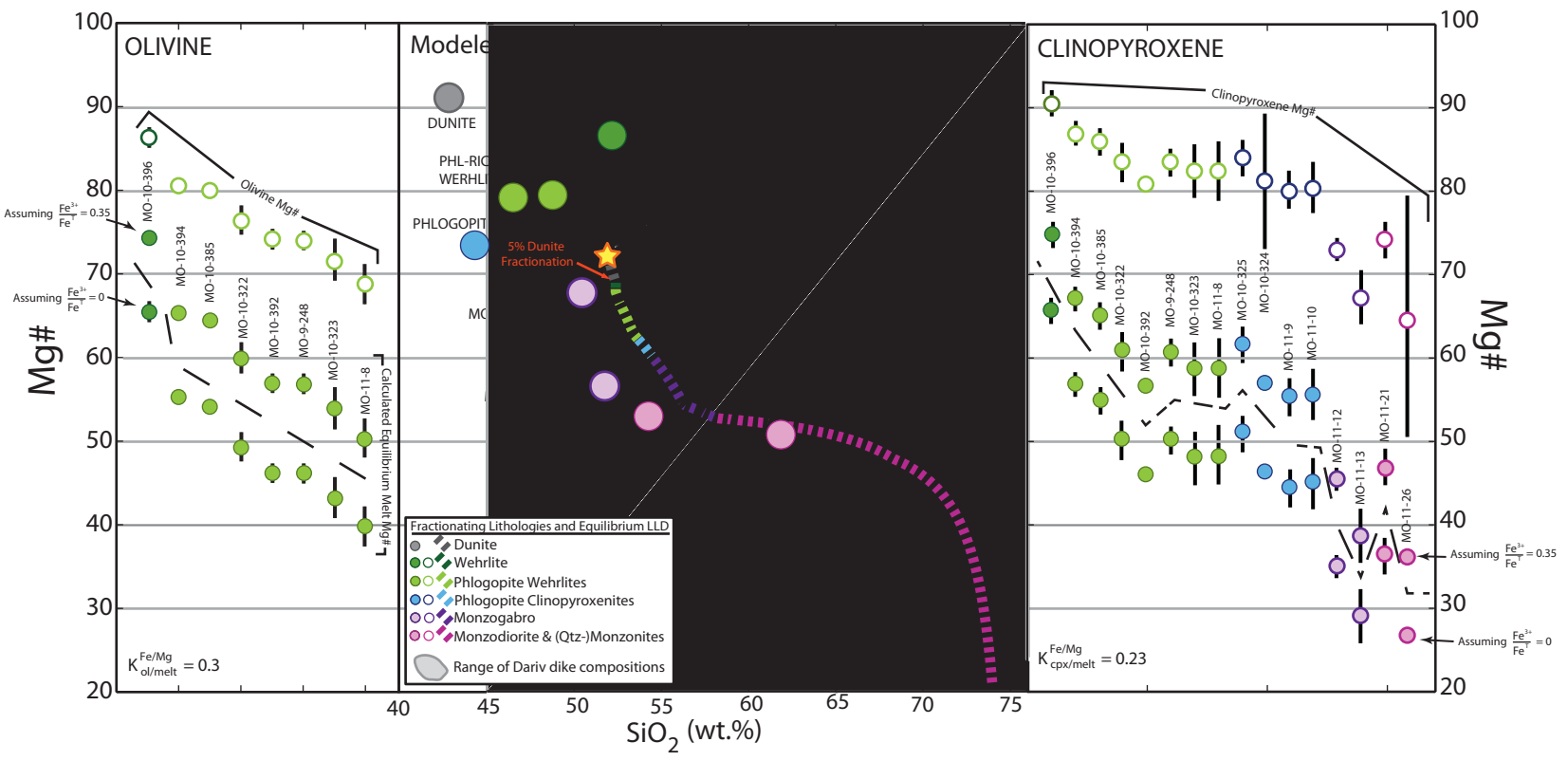
OLIVINE
Olivine Mg#
Assuming $\frac{Fe^{3+}}{Fe^{T}} = 0.35$
Assuming $\frac{Fe^{3+}}{Fe^{T}} = 0$
MO-10-396
MO-10-394
MO-10-385
MO-10-322
MO-10-392
MO-9-248
MO-10-323
MO-11-8
Calculated Equilibrium Melt Mg#
$K^{Fe/Mg}_{ol/melt} = 0.3$
Modele
DUNITE
PHL-RIC
WERHLI
PHLOGOPIT
MC
5% Dunite Fractionation
Fractionating Lithologies and Equilibrium LLD
Dunite
Wehrlite
Phlogopite Wehrlites
Phlogopite Clinopyroxenites
Monzogabro
Monzodiorite & (Qtz-)Monzonites
Range of Dariv dike compositions
CLINOPYROXENE
Clinopyroxene Mg#
MO-10-396
MO-10-394
MO-10-385
MO-10-322
MO-10-392
MO-9-248
MO-10-323
MO-11-8
MO-10-325
MO-10-324
MO-11-9
MO-11-10
MO-11-12
MO-11-13
MO-11-21
MO-11-26
Assuming $\frac{Fe^{3+}}{Fe^{T}} = 0.35$
Assuming $\frac{Fe^{3+}}{Fe^{T}} = 0$
$K^{Fe/Mg}_{cpx/melt} = 0.23$
Mg#
$SiO_2$ (wt.%)
100
90
80
70
60
50
40
30
20
40
45
50
55
60
65
70
75

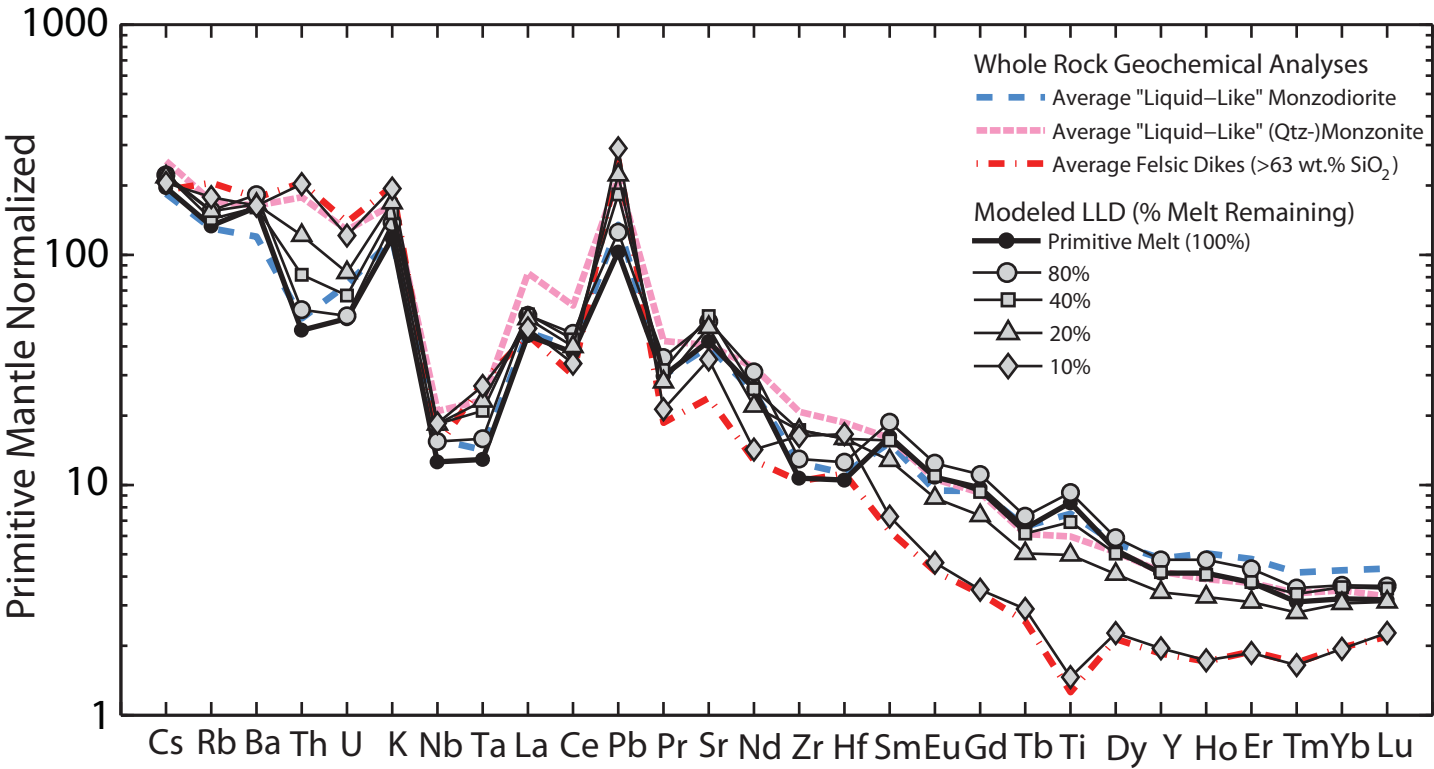
Primitive Mantle Normalized
1000
100
10
1
Cs Rb Ba Th U K Nb Ta La Ce Pb Pr Sr Nd Zr Hf Sm Eu Gd Tb Ti Dy Y Ho Er Tm Yb Lu
Whole Rock Geochemical Analyses
Average "Liquid–Like" Monzodiorite
Average "Liquid–Like" (Qtz-)Monzonite
Average Felsic Dikes (>63 wt.% SiO2)
Modeled LLD (% Melt Remaining)
Primitive Melt (100%)
80%
40%
20%
10%

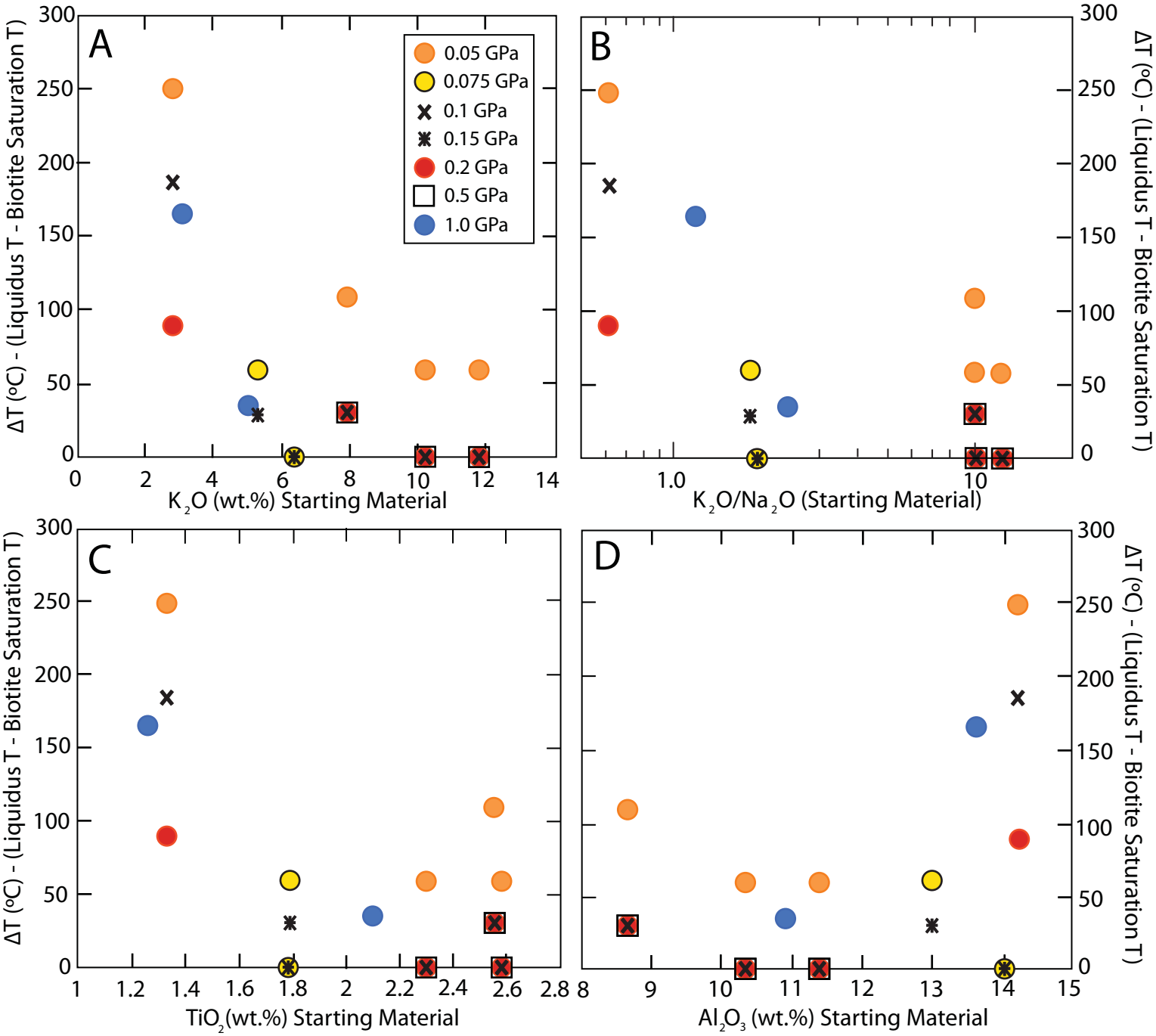
A
B
C
D
0.05 GPa
0.075 GPa
0.1 GPa
0.15 GPa
0.2 GPa
0.5 GPa
1.0 GPa
ΔT (ºC) - (Liquidus T - Biotite Saturation T)
K2O (wt.%) Starting Material
K2O/Na2O (Starting Material)
TiO2(wt.%) Starting Material
Al2O3 (wt.%) Starting Material

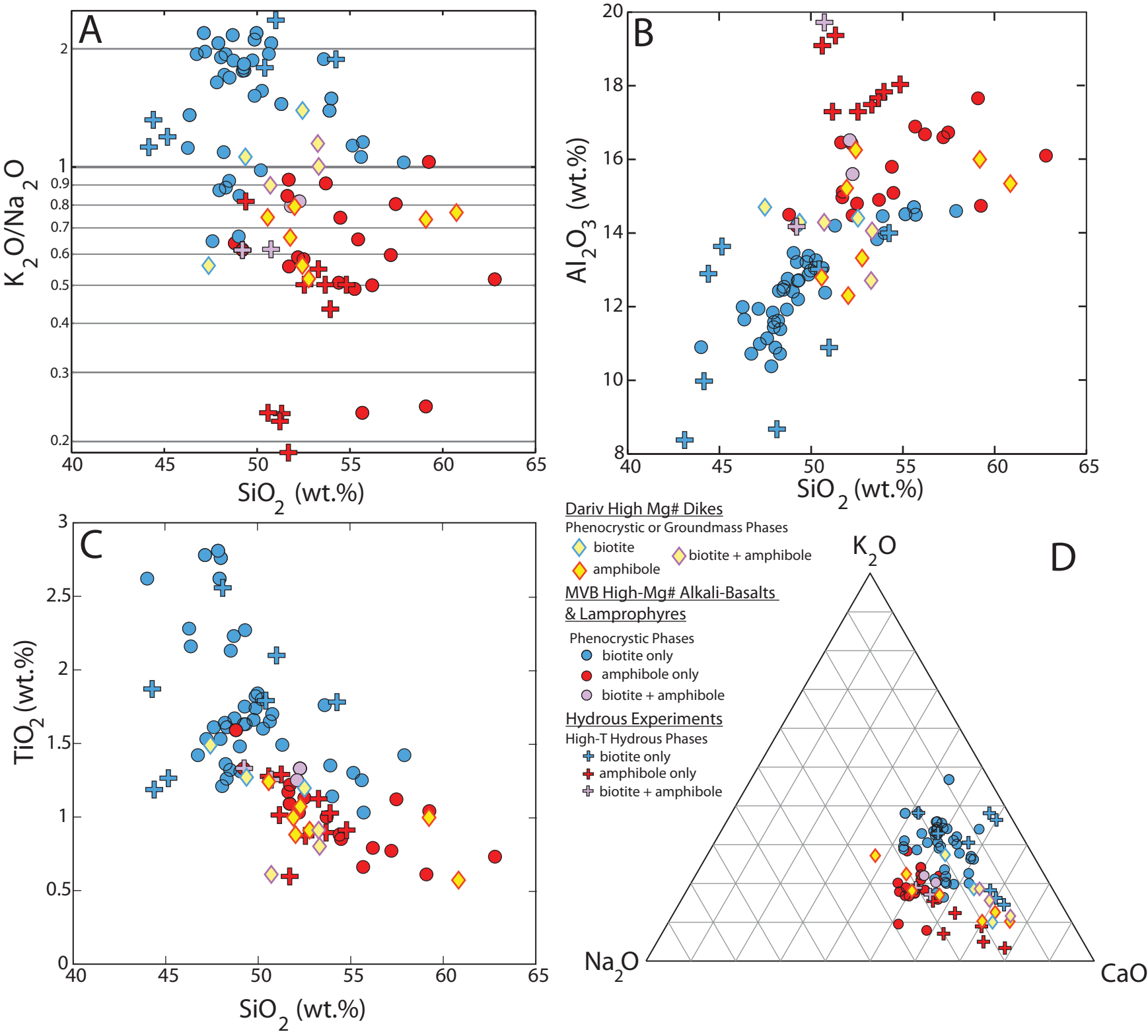
A
B
C
D
K2O/Na2O
SiO2 (wt.%)
Al2O3 (wt.%)
TiO2 (wt.%)
Dariv High Mg# Dikes
Phenocrystic or Groundmass Phases
biotite
amphibole
biotite + amphibole
MVB High-Mg# Alkali-Basalts & Lamprophyres
Phenocrystic Phases
biotite only
amphibole only
biotite + amphibole
Hydrous Experiments
High-T Hydrous Phases
biotite only
amphibole only
biotite + amphibole
K2O
Na2O
CaO

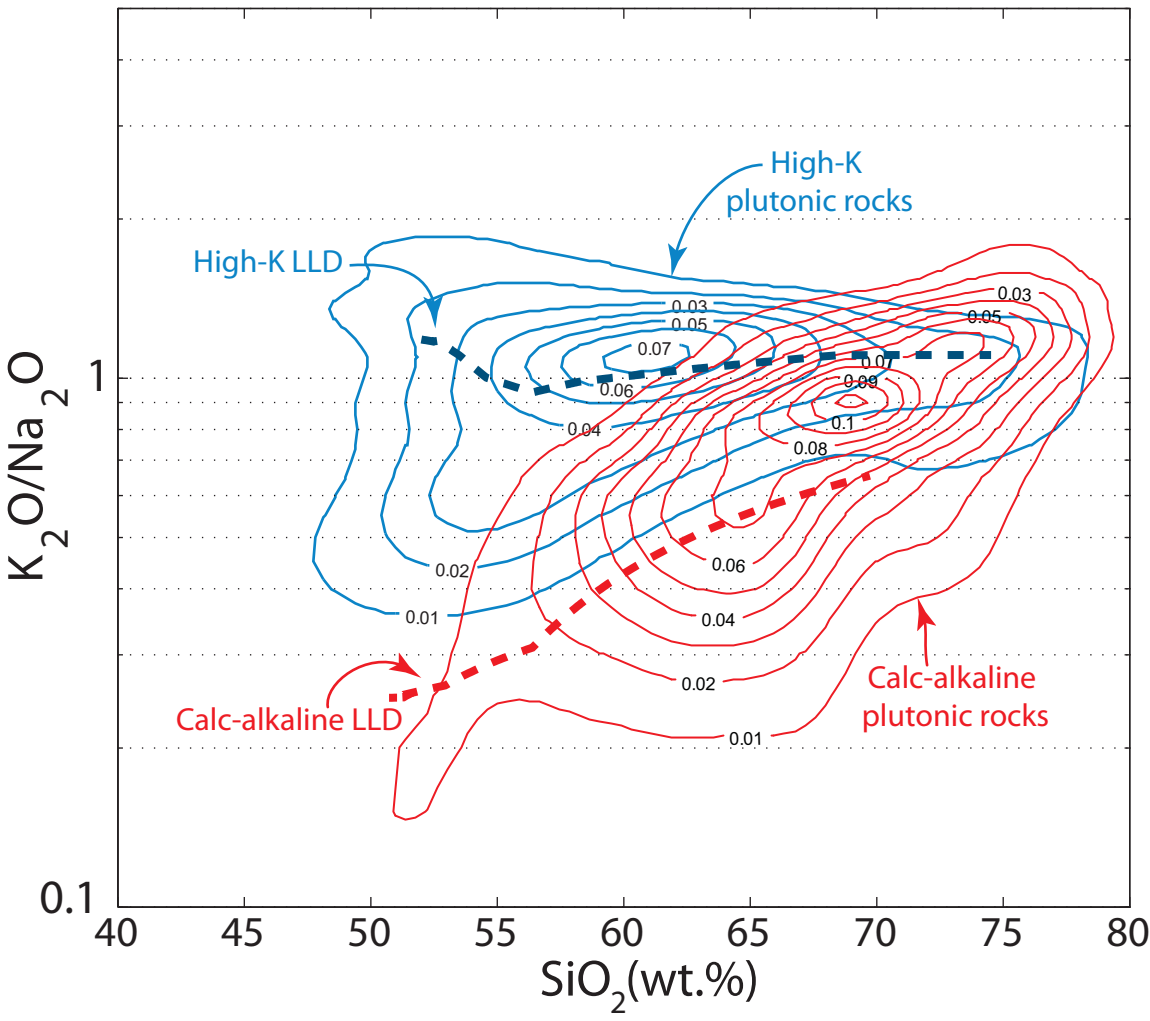
High-K
plutonic rocks
High-K LLD
0.03
0.05
0.07
0.06
0.04
0.02
0.01
0.09
0.1
0.08
Calc-alkaline LLD
Calc-alkaline
plutonic rocks
$K_2O/Na_2O$
1
0.1
40
45
50
55
60
65
70
75
80
$SiO_2$(wt.%)

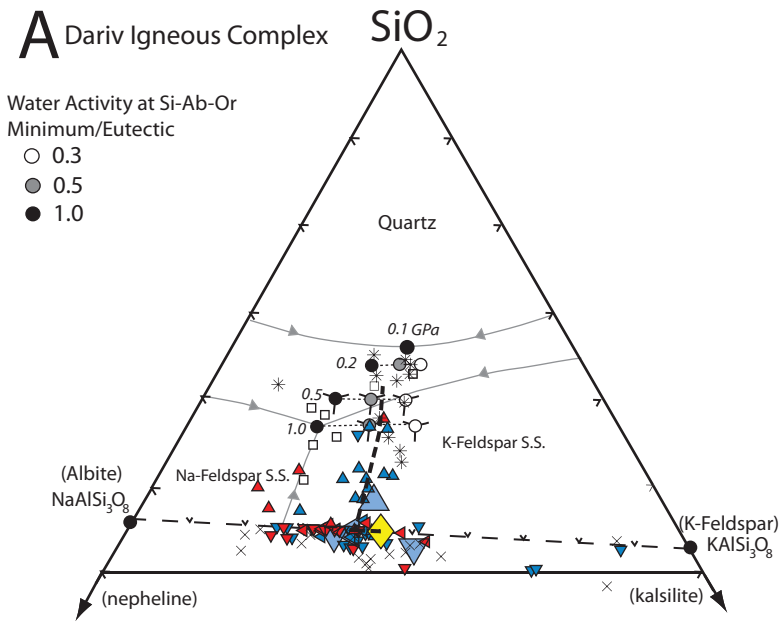
A Dariv Igneous Complex
SiO2
Water Activity at Si-Ab-Or Minimum/Eutectic
0.3
0.5
1.0
Quartz
0.1 GPa
0.2
0.5
1.0
K-Feldspar S.S.
Na-Feldspar S.S.
(Albite)
NaAlSi3O8
(K-Feldspar)
KAlSi3O8
(nepheline)
(kalsilite)

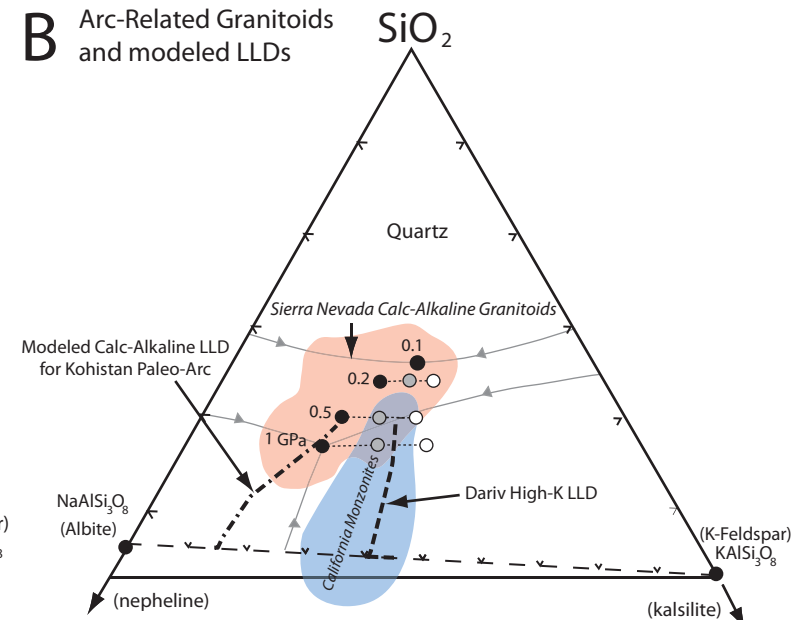
B Arc-Related Granitoids and modeled LLDs
SiO2
Quartz
Sierra Nevada Calc-Alkaline Granitoids
Modeled Calc-Alkaline LLD for Kohistan Paleo-Arc
0.1
0.2
0.5
1 GPa
Dariv High-K LLD
California Monzonites
NaAlSi3O8
(Albite)
(K-Feldspar)
KAlSi3O8
(nepheline)
(kalsilite)